

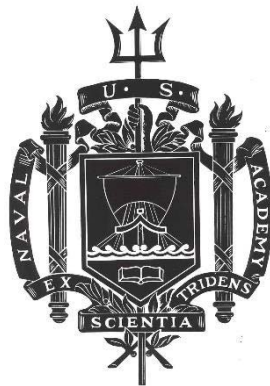
A TRIDENT SCHOLAR PROJECT REPORT

NO. 488

The Effects of Nanostructuring on the Thermal Transport of Electronic Materials

by

Midshipman 1/C Nicholas T. Vu, USN



UNITED STATES NAVAL ACADEMY
ANNAPOLIS, MARYLAND

This document has been approved for public
release and sale; its distribution is unlimited.

USNA-1531-2

REPORT DOCUMENTATION PAGE				Form Approved OMB No. 0704-0188	
Public reporting burden for this collection of information is estimated to average 1 hour per response, including the time for reviewing instructions, searching existing data sources, gathering and maintaining the data needed, and completing and reviewing this collection of information. Send comments regarding this burden estimate or any other aspect of this collection of information, including suggestions for reducing this burden to Department of Defense, Washington Headquarters Services, Directorate for Information Operations and Reports (0704-0188), 1215 Jefferson Davis Highway, Suite 1204, Arlington, VA 22202-4302. Respondents should be aware that notwithstanding any other provision of law, no person shall be subject to any penalty for failing to comply with a collection of information if it does not display a currently valid OMB control number. PLEASE DO NOT RETURN YOUR FORM TO THE ABOVE ADDRESS.					
1. REPORT DATE (DD-MM-YYYY) 5-20-19		2. REPORT TYPE		3. DATES COVERED (From - To)	
4. TITLE AND SUBTITLE The Effects of Nanostructuring on the Thermal Transport of Electronic Materials				5a. CONTRACT NUMBER	
				5b. GRANT NUMBER	
				5c. PROGRAM ELEMENT NUMBER	
6. AUTHOR(S) Vu, Nicholas T.				5d. PROJECT NUMBER	
				5e. TASK NUMBER	
				5f. WORK UNIT NUMBER	
7. PERFORMING ORGANIZATION NAME(S) AND ADDRESS(ES)				8. PERFORMING ORGANIZATION REPORT NUMBER	
9. SPONSORING / MONITORING AGENCY NAME(S) AND ADDRESS(ES) U.S. Naval Academy Annapolis, MD 21402				10. SPONSOR/MONITOR'S ACRONYM(S)	
				11. SPONSOR/MONITOR'S REPORT NUMBER(S) Trident Scholar Report no. 488 (2019)	
12. DISTRIBUTION / AVAILABILITY STATEMENT This document has been approved for public release; its distribution is UNLIMITED.					
13. SUPPLEMENTARY NOTES					
14. ABSTRACT Understanding the fundamental energy transport mechanisms in nanostructured materials is vital to the development of smaller, energy-dense systems. This is particularly important in materials used in high power density electronic systems and renewable energy platforms, where performance is directly tied to the thermal properties of constituent materials. By altering the nanostructure, the thermal properties can be tailored to meet various needs. Frequency Domain Thermorefectance (FDTR), an optical pump-probe thermal characterization technique, is used to characterize the thermal properties of different electronic materials. An FDTR system was built as part of this project and validated with reference scans of known materials. This work thermally characterizes nickel titanium (NiTi), germanium telluride (GeTe), Bi ₂ Te ₃ /Bi ₂ (TeSe) ₃ superlattices, and gallium nitride (GaN). NiTi is a candidate material for elastocaloric cooling and thermal energy storage applications. We show that increasing the grain size of NiTi significantly increases thermal conductivity on both sides of the phase change. We study the impact of film thickness on the thermal conductivity of the crystalline and amorphous phases of germanium telluride (GeTe). It was found that the mean free path of heat energy carriers is similar in both phases of the material. The application of a phonon scattering model to a thickness-dependent thermal conductivity dataset indicates that phonon boundary scattering is the predominant physical mechanism that limits thermal transport in thin-films of GeTe. Superlattices with alternating thin-films of Bi ₂ Te ₃ and Bi ₂ (TeSe) ₃ were thermally characterized. We find a large degree of thermal anisotropy and a significant increase in the in-plane thermal conductivity compared to bulk values, possibly due to a topological insulator effect. We report preliminary results of the thermal conductivity of seed-grown GaN films with a grain size gradient on partially etched substrates.					
15. SUBJECT TERMS FDTR, NiTi, GeTe, GaN, Superlattices, Bismuth Telluride, Nanoscale Heat Transfer					
16. SECURITY CLASSIFICATION OF:			17. LIMITATION OF ABSTRACT	18. NUMBER OF PAGES 73	19a. NAME OF RESPONSIBLE PERSON
a. REPORT	b. ABSTRACT	c. THIS PAGE			19b. TELEPHONE NUMBER (include area code)

U.S.N.A. --- Trident Scholar project report; no. 488 (2019)

**THE EFFECTS OF NANOSTRUCTURING ON THE
THERMAL TRANSPORT OF ELECTRONIC MATERIALS**

by

Midshipman 1/C Nicholas T. Vu
United States Naval Academy
Annapolis, Maryland

(signature)

Certification of Advisers Approval

Assistant Professor Ronald J. Warzoha
Mechanical Engineering Department

(signature)

(date)

Professor Andrew N. Smith, USN
Mechanical Engineering Department

(signature)

(date)

Assistant Professor Brian F. Donovan, USN
Physics Department

(signature)

(date)

Acceptance for the Trident Scholar Committee

Professor Maria J. Schroeder
Associate Director of Midshipman Research

(signature)

(date)

Abstract

Understanding the fundamental energy transport mechanisms in nanostructured materials is vital to the development of smaller, energy-dense systems. This is particularly important in materials used in high power density electronic systems and renewable energy platforms, where performance is directly tied to the thermal properties of constituent materials. By altering the nanostructure, the thermal properties can be tailored to meet various needs.

Frequency Domain Thermoreflectance (FDTR), an optical pump-probe thermal characterization technique, is used to characterize the thermal properties of different electronic materials. An FDTR system was built as part of this project and validated with reference scans of known materials.

This work thermally characterizes nickel titanium (NiTi), germanium telluride (GeTe), $\text{Bi}_2\text{Te}_3/\text{Bi}_2(\text{TeSe})_3$ superlattices, and gallium nitride (GaN). NiTi is a candidate material for elastocaloric cooling and thermal energy storage applications. We show that increasing the grain size of NiTi significantly increases thermal conductivity on both sides of the phase change. We study the impact of film thickness on the thermal conductivity of the crystalline and amorphous phases of germanium telluride (GeTe). It was found that the mean free path of heat energy carriers is similar in both phases of the material. The application of a phonon scattering model to a thickness-dependent thermal conductivity dataset indicates that phonon boundary scattering is the predominant physical mechanism that limits thermal transport in thin-films of GeTe. Superlattices with alternating thin-films of Bi_2Te_3 and $\text{Bi}_2(\text{TeSe})_3$ were thermally characterized. We find a large degree of thermal anisotropy and a significant increase in the in-plane thermal conductivity compared to bulk values, possibly due to a topological insulator effect. We report preliminary results of the thermal conductivity of seed-grown GaN films with a grain size gradient on partially etched substrates. Keywords: FDTR, NiTi, GeTe, GaN, Superlattices, Bismuth Telluride, Nanoscale Heat Transfer

Acknowledgements

I would first like to thank my primary adviser, Prof. Warzoha. There is not a professor who has his level of dedication to his students. There were many days where we were both in the lab well past midnight trying to figure out a problem. I don't know how that man works so hard, but his tenacity and passion for learning has always been an inspiration for me. I would not have made it without his continual mentorship throughout the project, helping me navigate the complicating topic of nanoscale heat transfer and helping me make big life decisions.

I would next like to thank Prof. Smith. I have known him since Plebe year, as he was my academic adviser. He helped me navigate my unorthodox course load, and he was the one who got me started with the Trident process. Prof. Smith throughout this project served as the realist and paternal figure, helping ground us when we got too excited or reminding me when I was unsafe with laser safety goggles or seatbelts in Chinese taxicabs.

Third, I would like to thank Prof. Donovan. He is definitely one of the smartest people I know, especially with regards to nanoscale heat transfer. His excitement on the subject is infectious. He has helped with every aspect of the project, for which I am grateful.

I would also like to acknowledge our many collaborators and financial supporters. Dr. Sharar, Dr. Leff, Dr. Wilson, and Dr. Taylor from Army Research Laboratory have helped with the NiTi and superlattice studies. Dr. Champlain, Dr. Mack, Dr. Ruppalt, Dr. Koehler, and Dr. Tadjer from the Navy Research Laboratory helped with the GeTe and GaN studies. Dr. Mark Spector and Mr. Peter Morrison from the Office of Naval Research have provided their continual support to the research performed in the lab.

Finally, I would like to thank my family and friends for their help. Thank you Mom, Dad, and Chris for being there from the start. Thank you to my good friend Monika for providing emotional and nutritional support. I would also like to give special shout out to my roommates Austin, Cedric, and Jordan for always being there for me.

Contents

Abstract	1
Acknowledgements	2
List of Figures	4
List of Tables	7
Introduction	8
1 Introduction to Nanoscale Heat Transfer	10
1.1 Phonon Heat Transfer	11
1.1.1 Particle Picture of Phonons	11
1.1.2 Wave Picture of Phonons	13
1.1.3 The Calloway Model	14
1.2 Electron Contribution to Thermal Conductivity	15
2 Frequency Domain Thermorefectance	16
2.1 Experimental Setup	18
2.2 Theory	20
2.3 System Validation with Reference Materials	23
3 Nickel Titanium Shape Memory Alloys	27
3.1 Fabrication and Microscopy	30
3.2 Results and Analysis	33
3.3 Conclusions	35
4 Germanium Telluride	36
4.1 Material Synthesis and Physical Characterization	37

4.2	Results and Discussion	38
4.3	Conclusions	41
5	Bi₂Te₃/Bi₂(TeSe)₃ Superlattices	43
5.1	Sample Set and Microscopy	45
5.2	Results and Discussion	46
5.3	Conclusions	48
6	Gallium Nitride	49
6.1	Material Stack	50
6.2	Results and Discussion	50
6.3	Conclusions	53
	Conclusions	54
	References	56
	Appendices	64
	Appendix A FDTR Progression	64
	Appendix B Projected Publications and Presentations	72
B.1	Projected Publications	72
B.2	Conference Presentations	73

List of Figures

1.1	Phonon mass-spring model.	13
2.1	The top diagram shows the input power from the pump (blue) and the temperature response of the surface (green). The bottom diagram shows the input intensity of the pump and the measured intensity of the probe.	16

2.2	Coefficient of Thermorefectance at different wavelengths for common trans- ducers [1].	18
2.3	FDTR setup.	19
2.4	(a) FDTR solution for SiO_2 . (b) Sensitivity plot for SiO_2 . (c) FDTR solution for Al_2O_3 . (d) Sensitivity plot for Al_2O_3 . (e) FDTR solution for Si. (f) Sensitivity plot for Si.	25
2.5	Measured thermal conductivity of sapphire as a function of temperature. These values are compared with values retrieved from Cahill [2].	26
3.1	(a) Elastocoloric cooling cycle using the austenitic-martensitic phase trans- formation of SMAs. (b) A traditional vapor-compression refrigeration cycle. As shown from the two cycles, many of the principles are similar, such as the presence of two phases (solid-solid vs. liquid-vapor) and a form of stress applied (strain vs. compression).	28
3.2	TE bright field TEM micrograph of AR specimen showing: (a) representative region of NiTi microstructure, (b) large, single crystal Ti inclusion, and (c) %Ti EDS map of Ti inclusion, where white is 100%, suggesting that the inclusions were pure Ti.	30
3.3	[001] inverse pole map obtained from EBSD of 3 min annealed sample, which determined grain size to be $39 \pm 10 \mu\text{m}$ and showed textured B2 austenite and R-phase' martensite.	31
3.4	(a) Bright field TEM micrograph showing R-Phase grain adjacent to two B2 Austenite grains. (b) Absolute background filtered HRTEM micrograph from the same R-phase grain. The image shows a 0.635 nm periodic spacing be- tween $[10\bar{1}0]$ planes. (c) $[\bar{2}021]$ zone axis selected area diffraction pattern for same R-phase grain.	32

3.5	[001] inverse pole map obtained from EBSD of 5 min annealed sample, which determined grain size to be $56 \pm 13 \mu\text{m}$ and showed textured B2 austenite and R-phase' martensite.	32
3.6	(a) Bright field TEM micrograph showing the interface between two B2 Austenite grains. (b) Absolute background filtered HRTEM micrograph from the upper grain in (a). (c) [111] zone axis selected area diffraction pattern for same R-phase grain.	33
3.7	Example FDTR result and sensitivity plot of a 30s annealed sample.	33
3.8	Thermal conductivity as a function of temperature for the nanograined as-received sample ($\langle d \rangle = 40 \pm 30 \text{ nm}$), the 3 min annealed sample ($\langle d \rangle = 39 \pm 10 \mu\text{m}$), and the 5 min annealed sample ($\langle d \rangle = 56 \pm 13 \mu\text{m}$).	34
4.1	(a) FDTR scans and curve fits for thickest c-GeTe and a-GeTe samples. (b) Sensitivity plot of the thickest c-GeTe sample.	39
4.2	κ as a function of film thickness for c-GeTe and a-GeTe.	40
5.1	Diagram of Superlattice Material Stack.	45
5.2	(a) HRTEM of the interface between the superlattice and Bi_2Te_3 buffer. (b) HRTEM of the interface between the Bi_2Te_3 buffer and GaAs substrate. . . .	46
5.3	In-plane and cross-plane thermal conductivity of $\text{Bi}_2\text{Te}_3/\text{Bi}_2(\text{TeSe})_3$ as a function of electrical resistance.	47
6.1	Diagram of the GaN material stack. These materials were etched on the bottom and coated with the transducer on both sides. This allows the measurement from the top and bottom.	50
6.2	FDTR Scans and Curve Fits for GaN material stack.	51
6.3	(a) Sensitivity plot of GaN stack measured from the top over the etch. (b) Sensitivity plot of GaN stack measured from the top over the substrate. . . .	52
A.1	Image of the bare optical table.	64
A.2	Original FDTR setup with 532 nm probe, 808 nm pump.	65

A.3	Old FDTR scan of Si with a large amount of noise.	66
A.4	Old FDTR scan of SiO ₂ with a large amount of noise.	67
A.5	Old FDTR scan with noise fixes.	67
A.6	FFT of signal from the Millenia eV5.	68
A.7	(a) FDTR scan of Si from using the Millenia eV10. (b) FDTR scan of SiO ₂ using the Millenia eV10.	69
A.8	(a) XYZ stage inside of cryostat. (b) Periscope mount used to probe down into cryostat.	69
A.9	FDTR scan of Silicon.	70
A.10	Optical Table at the time of this report.	71

List of Tables

1.1	Phonon scattering terms and associated mathematical form.	13
2.1	Measured thermal conductivity values of reference samples compared with literature.	24
3.1	Measured thermal conductivities of NiTi and associated temperature range. .	29
4.1	GeTe target and measured film thicknesses.	38
5.1	Overview of the three Bi ₂ Te ₃ /Bi ₂ (TeSe) ₃ superlattices configurations studied.	45
5.2	In-plane and cross-plane thermal conductivity and electrical resistivity of the Bi ₂ Te ₃ /Bi ₂ (TeSe) ₃ superlattice configurations studied. The anisotropy ratios and effective Lorenz numbers were also calculated.	46
6.1	Assumed and measured properties used to fit the GaN data.	51
6.2	Regressed parameters for GaN material stack	52

Introduction

Thermal management is a significant concern for the successful operation of many of the technologies we use today. This is especially true with decreasing component footprints and increasing energy densities of many micro-scale and nano-scale technologies. As the size of these technologies approach the characteristic length scales of the energy carriers, many of the classical laws that define energy transport at the macroscale (i.e. $<100\text{nm}$) begin to break down, causing unexpected temperature excursions that could negatively impact device performance [3]. By understanding the fundamental energy transport mechanisms at the nanoscale, we can gain more insight on device behavior in application. Moreover, this knowledge may allow us to alter the nanostructure of materials to tailor the thermal properties and meet the requirements of various applications.

For the work presented in this report, we interrogate the effects of nanostructuring on the thermal properties of four different materials important to a variety of electronic applications. The first material studied was Nickel Titanium, a shape memory alloy that can be used for solid-state refrigeration [4] and thermal energy storage [5]. For this material, we examine the effects of changing grain size on thermal conductivity on each side of a solid-state phase transition. Next, nanoscale energy transport within Germanium Telluride (GeTe), a phase change material used for non-volatile memory [6] and various optical applications [7,8], was investigated. For this material, we altered the film thickness from 30 nm-1200 nm to determine the length scales of the dominant energy carriers to better understand their impacts on thermal conductivity. Measurements were made on GeTe in both the crystalline and amorphous phase. The third material studied was a $\text{Bi}_2\text{Te}_3/\text{Bi}(\text{TeSe})_3$ superlattice, which is a material that is typically used for thermoelectric energy generation [9] and as a topological insulator [10]. For these materials, we explore the effects of stacking unique materials on thermal conductivity, with special consideration to its effects on thermal anisotropy. Finally, we examine thermal transport on the top and bottom side of seed-grown Gallium Nitride

(GaN), a material used for optoelectric devices, high efficiency power amplifiers, and power electronics [11]. We study the thermal conductivity of seed-grown GaN films with partially etched substrates having a grain size gradient in the through-thickness direction. Thermal conductivity measurements have been made on the top side in agreement with literature. We expect to find a disparity between the thermal conductivity of the two sides.

Characterization of thermal properties throughout this study was primarily achieved using Frequency Domain Thermoreflectance (FDTR), a non-contact optical pump-probe thermal technique. As part of this project, a custom FDTR system was built.

This report will be divided into six chapters. The first will provide a basic explanation of nanoscale heat transfer principles and the analytical formulations used to gain insight into the physical mechanisms that govern thermal transport in the nanoengineered materials examined. The second chapter discusses FDTR, including the theoretical background, experimental setup used for the completion of the project, and validation of the accuracy of the technique for characterizing thermal properties using bulk reference materials. Finally, chapters three through six discuss the background and results for the studies on Nickel Titanium, Germanium Telluride, $\text{Bi}_2\text{Te}_3/\text{Bi}(\text{TeSe})_3$ superlattices, and Gallium Nitride.

Also included are two appendices. The first appendix discusses the process of setting up the FDTR system. The setup proved to be much more of a challenge than expected, and a large amount of time in this project was spent making improvements to the system layout and design. The second appendix lists the publications that have been submitted or are expected to result from this work, along with details regarding conference presentations related to this project.

1 Introduction to Nanoscale Heat Transfer

This report will only focus on the aspects of nanoscale heat transfer that apply to the material systems we studied. Additional background information can be found in textbooks such as Chen [3], Kittel et al. [12], and Incropera et al. [13].

Heat conduction is the transfer of thermal energy through a stationary medium, resulting from a temperature gradient in the material [3]. This is often modeled with Fourier's law, which states:

$$\mathbf{q} = -\kappa \nabla T. \quad (1.1)$$

where \mathbf{q} is the heat flux, κ is the thermal conductivity, and ∇T is the temperature gradient. The thermal conductivity is a fundamental material property that defines how well a material can conduct heat.

Most solids are crystalline, which means that the material is comprised of atoms and electrons bound periodically in a lattice [12]. Thermal transport through these materials is caused both by the vibrations through the lattice about their equilibrium positions and the movement of free electrons.

The equilibrium position for the atoms in the lattice is where the repulsion energy balances the attraction energy of neighboring atoms. The atoms attract because the negatively charged electron orbitals of one atom attracts the nucleus of a neighboring atom, and they repel once the atoms become close enough for the like charges between neighboring electrons and nuclei to interact. All of the atoms in the lattice vibrate around this position, and hotter atoms vibrate with larger amplitudes. Due to interatomic interactions, the increase in vibrational amplitude of these hotter atoms propagate through the crystal as waves, leading to a net transfer of heat from hot to cold. These vibrations in solids are treated as quasi-particles known as a phonons. Phonon heat transfer is the predominant transport mechanism for electrically insulating materials and semiconductors, while electrons dominate thermal transport within metals. The total thermal conductivity is the sum of the

phonon and electron contribution to thermal conductivity. This can be seen in Eqn. 1.2.

$$\kappa_T = \kappa_e + \kappa_p \quad (1.2)$$

I will first focus on the phonon contribution to heat transfer before moving into a brief discussion on the electron contribution to heat transfer in metallic systems.

1.1 Phonon Heat Transfer

Due to the wave-particle duality of matter, phonons can be treated as both waves and particles [3]. I will discuss the principles behind the particle picture and wave picture of the energy carriers. I will then discuss how the particle and wave pictures are used in the Calloway model, a simple yet effective model that describes thermal conductivity based on phonon transport mechanisms.

1.1.1 Particle Picture of Phonons

In the particle picture of the heat carriers, phonons are treated as a gas, and the heat transfer can be predicted based on the net energy transfer resulting from the random collisions between carriers. This simple gas model to describe phonon transport is based on kinetic theory and is commonly used to analyze material systems at length scales relevant to the materials studied in this work. As the energy carriers move randomly throughout the system, each phonon has an average velocity, v , and relaxation time, τ . For phonons, v is the speed of sound through the material, and τ is the average time a phonon travels before scattering and losing its excess energy.

This product of the v and τ gives the average distance traveled before scattering, which is known as the mean free path and denoted as Λ .

A good approximation for the the phonon thermal conductivity can be derived from

simple kinetic theory and Fourier's law, which results in

$$\kappa_{ph} = \frac{1}{3}C_v v^2 \tau = \frac{1}{3}C_v v \Lambda \quad (1.3)$$

where C_v is the volumetric heat capacity, the product of density and mass specific heat capacity [3].

The collision frequency, and therefore Λ , is affected by a variety of scattering mechanisms. For example, phonons can interact with other phonons, boundaries, defects, and grain boundaries [14]. Phonon-phonon scattering can either undergo normal scattering, which is where crystal momentum is conserved, or Umklapp scattering, which is where crystal momentum is not conserved [3]. Phonon Umklapp scattering is the phonon-phonon scattering mechanism that impacts κ at a rate proportional to $1/T$ and is typically the predominant scattering mechanism at higher temperatures [12]. At lower temperatures, boundary scattering and defect scattering become the dominant scattering mechanisms [14, 15]. Boundary scattering becomes a dominant scattering mechanism when the mean free path approaches the characteristic length, which is more common in thin films and low temperatures where a decrease in phonon population density increases the mean free path [14, 15]. Defect scattering occurs when phonons interact with impurities, interstitials, and vacancies. These defects could be inherent or increased through a process such as doping [14].

The total τ is ultimately the combination of the contributions from all of the scattering mechanisms expected to occur within a particular material system. These can be combined using Matthiessen's rule:

$$\frac{1}{\tau} = \frac{1}{\tau_1} + \frac{1}{\tau_2} + \dots \frac{1}{\tau_n} \quad (1.4)$$

The phonon scattering terms that are important in this study are shown below in Table 1.1.

Table 1.1: Phonon scattering terms and associated mathematical form.

Scattering Mechanism	Factor	Mathematical Form	Reference
Phonon-Phonon	$\frac{1}{\tau_{Ph}}$	$AT\omega^2 \exp(\frac{-B}{T})$	[15, 16]
Boundary	$\frac{1}{\tau_{Bound}}$	$\frac{v}{d_{film}}$	[16, 17]
Grain Boundary	$\frac{1}{\tau_{Grain}}$	$\frac{v}{d_{gb}}$	[16, 18]

1.1.2 Wave Picture of Phonons

The atoms in the lattice can be treated as a mass-spring model, where the atom is connected to neighboring atoms and oscillates around its equilibrium value. This can be seen in Figure 1.1.

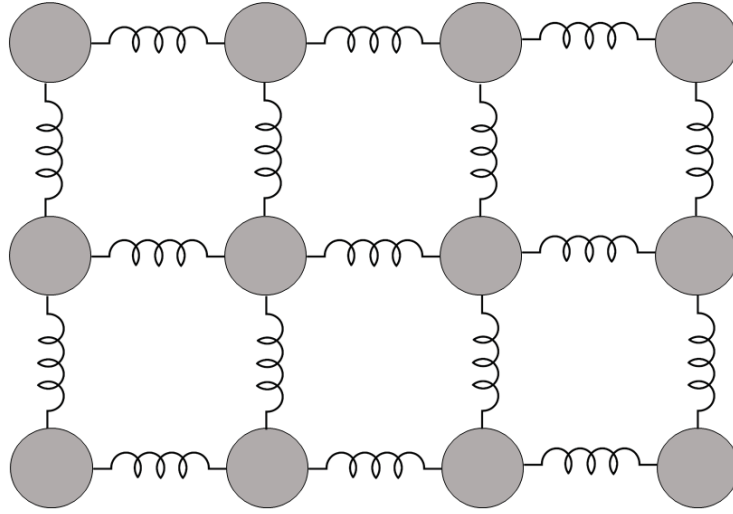


Figure 1.1: Phonon mass-spring model.

From this mass-spring model, we can see how vibrations in one atom would cause vibrations in neighboring atoms and propagate throughout the material. These propagations through the material could be longitudinal, which are compressions and expansions in the direction of wave propagation, or transverse, which are translations in the directions normal to the direction of wave propagation. For every atom, there is one longitudinal mode and two transverse modes.

Each of these atoms also vibrate at specific frequencies, wavelengths, and an amplitude that lies within discrete energy levels. Acoustic phonons are in-phase displacements that operate in the lower frequency modes, while optical phonons are out of phase oscillations (i.e. atoms in the lattice moving in different directions) that occur at higher frequencies. The wavelength is determined by the boundaries and atomic spacing. The allowable energy is a function of the wavevector, \mathbf{k} , which is in the direction of the wave propagation and has a magnitude of 2π divided by wavelength. This energy value is a multiple of the phonon frequency multiplied by Planck's constant.

By accounting for the different energy states in the material system, we can determine the heat capacity of the material. To do so, we need to account for all of the potential phonon modes, which is determined by the phonon density of states, which is a function of frequency, and we need to account for the probability of each mode, which can be determined by the well-established Bose-Einstein distribution [3, 12].

The heat capacity can therefore be determined by

$$C = \int_0^{\omega_D} \hbar\omega \text{DOS}(\omega) \frac{dF_{BE}(\omega)}{dT} d\omega \quad (1.5)$$

where ω_d is the Debye frequency, \hbar is Plank's constant, ω is frequency, $\text{DOS}(\omega)$ is the phonon density of states as a function of frequency, F_{BE} is the Bose-Einstein distribution, and T is temperature. The Bose-Einstein distribution is defined as

$$F_{BE} = \frac{1}{\exp(\frac{\hbar V}{\kappa_B T}) - 1} \quad (1.6)$$

where κ_B is the Boltzmann's constant.

1.1.3 The Calloway Model

The Calloway model combines the particle nature of phonons to account for scattering and the wave nature of phonons to account for the heat capacity [15]. This leaves the following

equation for thermal conductivity:

$$\kappa_{ph} = \int_0^{\omega_d} \hbar \omega DOS(\omega) \frac{dF_{BE}(\omega)}{dT} v(\omega)^2 \tau(\omega) d\omega \quad (1.7)$$

1.2 Electron Contribution to Thermal Conductivity

The electron contribution for conductive materials can be estimated using the Wiedemann-Franz Law:

$$\kappa_e = \sigma LT \quad (1.8)$$

where σ is the electrical conductivity, L is the Lorenz number, and T is temperature [3]. L is roughly $2.45 \times 10^{-8} \text{ W}\Omega\text{K}^{-2}$, although it changes with different materials. For metals where electron transport dominates, the Wiedemann-Franz law is often used to estimate the thermal conductivity using electrical conductivity.

2 Frequency Domain Thermoreflectance

Frequency domain thermoreflectance (FDTR) was first proposed by Schmidt et al. in 2009, and since then, it has become an increasingly popular method of thermal characterization due to its accuracy and ability to simultaneously determine in-plane and through-plane thermal conductivity, volumetric heat capacity, and thermal boundary conductances between material layers in both nanoscale and bulk materials [19]. This technique is similar to time domain thermoreflectance (TDTR), but instead of varying time using a variable delay stage, FDTR varies frequency, which allows for a simpler setup [19].

FDTR measures the thermal properties by using two lasers: a modulated heat pump and a continuous probe. The pump beam serves as the heating source, while the probe beam measures the temperature response of the material through changes in reflectivity of the surface. When the material is heated, its temperature lags behind the applied heat. This can be seen in Figure 2.1, which is a representation of the phenomenon.

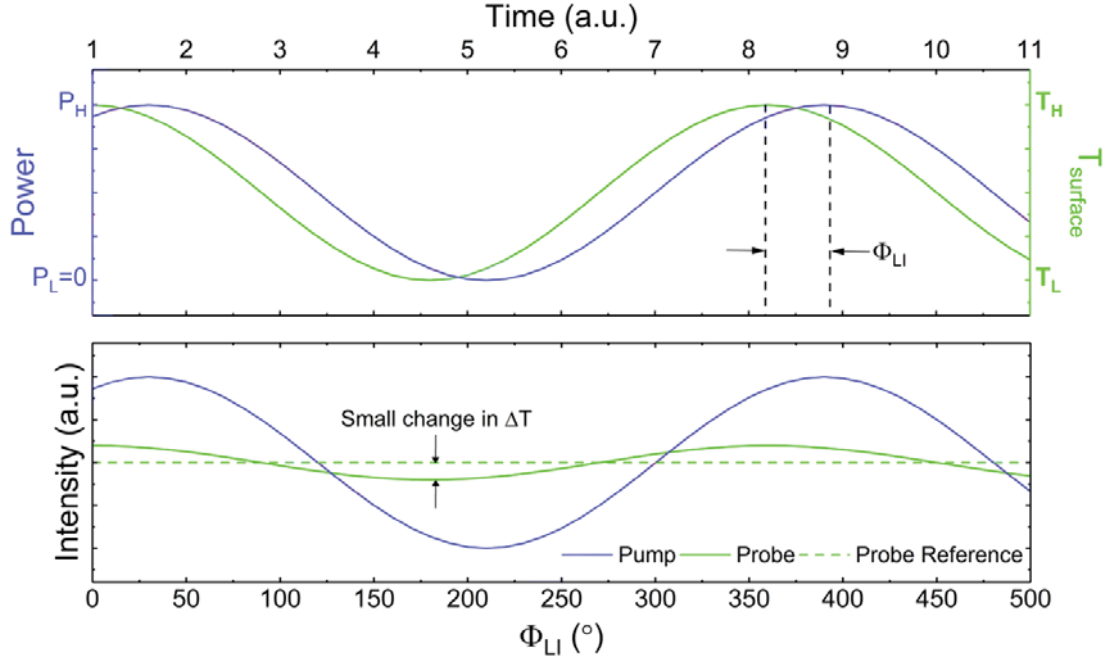


Figure 2.1: The top diagram shows the input power from the pump (blue) and the temperature response of the surface (green). The bottom diagram shows the input intensity of the pump and the measured intensity of the probe.

On the top diagram, the blue curve represents the power of the pump laser, which is modulating between P_L (low power) and P_H (high power). The corresponding temperature response of the surface is shown in green, which lags behind the applied temperature and fluctuates between T_L (low temperature) and T_H (high temperature). The difference in the phase between the pump and probe is the phase lag measured by the lock-in amplifier, ϕ_{LI} , and this provides information on the thermal properties of the material.

The bottom diagram in Figure 2.1 shows the intensity of the pump beam as well as the intensity of the reflected probe. The intensity and apparent modulation of the probe beam comes from the temperature response of the material induced by the pump. The intensity of the reflected probe depends on the surface reflectivity, which is proportional to the change in temperature depending on the coefficient of thermoreflectance. The probe reference that did not interact with the surface—and therefore remains unmodulated—is shown by the dotted green line. By subtracting the probe signal from the reference and taking into account the coefficient of thermoreflectance, the temperature response of the sample can be determined.

In order to obtain a strong coefficient of thermoreflectance, the sample is coated with a transducer by an electron beam evaporator. A transducer is chosen to strongly absorb the pump light while having a strong coefficient of thermoreflectance at the wavelength used by the probe. The coefficient of thermoreflectances as a function of wavelength for the transducers used is shown below in Figure 2.2. For our setup, either a gold or aluminum transducer is used with a green (532 nm) or red (808 nm) probe beam respectively to obtain a strong thermoreflectance signal.

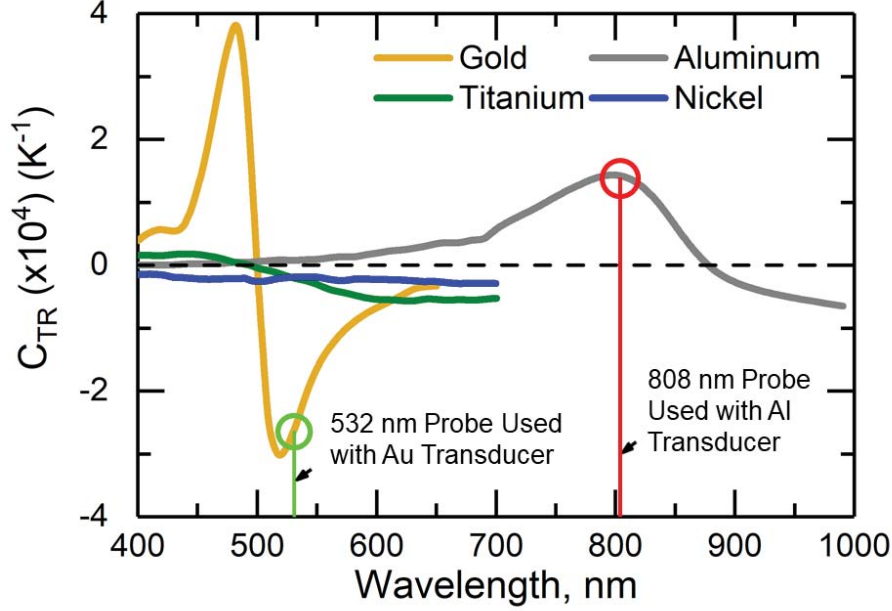


Figure 2.2: Coefficient of Thermoreflectance at different wavelengths for common transducers [1].

2.1 Experimental Setup

The FDTR setup used for this experiment follows the continuous wave FDTR setup proposed by Schmidt et al. [19] and improved by Yang [20]. The experimental procedure is also most similar to the alternate procedure for CW FDTR discussed in depth by Jiang et al. [21]. For our system, we have the ability to probe in both green (532 nm) and red (808 nm) depending on the transducer. Figure 2.3 shows the setup as configured for green. The red path is essentially the same and setup parallel to the green path with some different optics and a separate photodetector. Flip-mirrors are used to quickly switch between the two possible probe lasers.

For the green probe setup, the probe is a 532 nm CW diode laser (Coherent Obis LX). For the red probe setup, the probe is a 532 nm 10W laser (Millenia eV10) that sources a Ti-sapphire laser (Millenia 3900s), which converts the wavelength to 808 nm. The pump laser for both systems is a 405 nm CW diode laser (Coherent Obis LX). The pump is modulated by an electro-optic modulator (KD*P Series Model 350-160-01) that is driven by an output

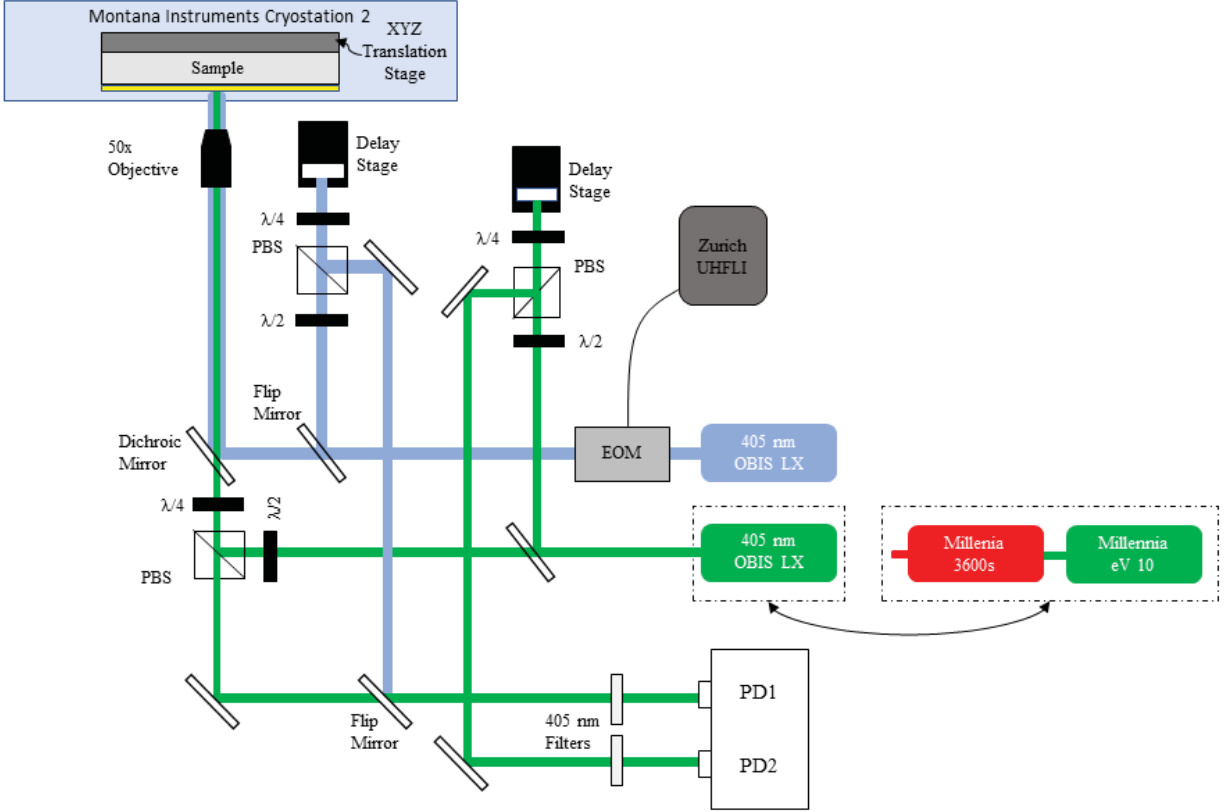


Figure 2.3: FDTR setup.

signal from the lock-in amplifier (Zurich UHFLI).

The pump laser is reflected by the dichroic mirror and focused onto the sample using an objective lens (Mitutoyo) at a magnification of 5x, 10x, 20x, or 50x. All of the data presented in this report was taken at a magnification of 20x. For room temperature measurements, the sample is mounted on an a translation stage and a tilt mount. For temperature dependent measurements, the samples are measured inside of a cryostat (Montana Instruments Cryostation 2) with an XYZ translation stage and a temperature mount (Agile Temperature Sample Mount) controlled by a temperature controller (Lakeshore Cryotronics Model 325 Temperature Controller). By using these components, we are able to rapidly control temperature with precision and move the sample in fine increments. In the future, we intend to use this XYZ stage for thermal microscopy using FDTR.

Before the dichroic mirror, the probe laser is split with a beam splitter. Half goes through

a half wave plate to rotate the beam 90 degrees, allowing it to be reflected by the polarized beam splitter (PBS) towards the sample. The probe beam rotates 45 more degrees by a quarter wave plate and reflects off the sample surface, picking up the modulation due to induced changes in reflectivity of the pump. The laser then goes back through the quarter wave plate, rotating the beam an additional 45 degrees for a total of 180 degrees. This allows the beam to go through the polarized beam splitter and reflect into photodetector 1 (PD1) of the balanced photodetector (Thorlabs PDB450A). The phase lag introduced by the sample is determined with a lock-in amplifier (Zurich UHFLI). This information in combination with a thermal model is used to determine the thermal properties of the sample.

The other half of the probe laser goes through a delay stage and into photodetector 2 (PD2) of the balanced photodetector. The delay stage is used to make this path length equidistant with the other half of the beam. PD2 is used to remove the noise of the probe beam from the signal detected with PD1. This will reduce the effects of any noise inherent in the laser.

The phase of the modulated source needs to be determined and subtracted from the measured phase signal of the probe to obtain the phase shift. In order to make this measurement the 405 nm filters are removed, the probe is shuttered, and the phase of the pump beam is measured at the highest frequency. This is possible because a small amount of the pump bleeds through the dichroic mirror. In order to make this measurement more efficiently, a reference pump beam is established. The path length of the pump reference is adjusted to match the phase at PD1 to the phase of the bleed through pump beam at PD1.

2.2 Theory

The theory behind FDTR follows the model proposed by Schmidt et al. [19] and is explained in detail by Yang [20].

To measure the thermal properties, the lock-in amplifier measures the harmonic component of the probe signal at ω_0 , the modulation frequency. The output of the lock-in amplifier

is the amplitude, A , and phase, ϕ , of the fundamental component of the probe signal with respect to the reference. The solution is expressed as a complex number, $Z(\omega_0)$, for reference wave $e^{i\omega_0 t}$:

$$Ae^{i(\omega_0 t + \phi)} = Z(\omega_0)e^{i\omega_0 t} \quad (2.1)$$

$Z(\omega_0)$ can be expressed by

$$Z(\omega_0) = \beta H(\omega_0) \quad (2.2)$$

where β is a function that has the sample thermorefectance coefficient and the power of the pump and probe beams and $H(\omega_0)$ is the thermal frequency of the sample weighted by the intensity of the probe beam. $H(\omega_0)$ is found by solving the heat diffusion equation for a Gaussian heat source striking a stack of materials and solving a two-dimensional heat conduction equation. The temperature distribution at the top is weighted by the Gaussian intensity distribution of the probe. The heat conduction equation for each layer in cylindrical coordinates is

$$\frac{\kappa_r}{r} \frac{\partial}{\partial r} \left(r \frac{\partial \theta}{\partial r} \right) + \kappa_z \frac{\partial^2 \theta}{\partial z^2} = C_v \frac{\partial \theta}{\partial t} \quad (2.3)$$

where κ_r is the in-plane thermal conductivity, θ is temperature, κ_z is the cross-plane thermal conductivity, and C_v is the volumetric heat capacity. Taking the Fourier transform and Hankel transform of Eqn. 2.3 results in

$$\kappa_z \frac{\partial^2 \theta(\omega, k, z)}{\partial z^2} = (\kappa_r k^2 + C_v i\omega) \theta(\omega, k, z) \quad (2.4)$$

where q is defined for a layer of material n and thickness d as

$$q^2 = \frac{\kappa_r k^2 + C_v i\omega}{\kappa_z} \quad (2.5)$$

We can relate the temperature and heat flux of the top surface, t , of a slab made of a certain material in the frequency domain with the bottom surface, b with

$$\begin{bmatrix} \theta_{n,b} \\ f_{n,b} \end{bmatrix} = \begin{bmatrix} \cosh(qd) & -\frac{1}{\kappa_z q} \sinh(qd) \\ -\kappa_z * q * \sinh(qd) & \cosh(qd) \end{bmatrix} \begin{bmatrix} \theta_{n,t} \\ f_{n,t} \end{bmatrix} \quad (2.6)$$

The temperature and heat flux between the bottom surface of material n are connected to the top of material $n + 1$ with

$$\begin{bmatrix} \theta_{n+1,t} \\ f_{n+1,t} \end{bmatrix} = \begin{bmatrix} 1 & -G^{-1} \\ 0 & 1 \end{bmatrix} \begin{bmatrix} \theta_{n,b} \\ f_{n,b} \end{bmatrix} \quad (2.7)$$

where G is the thermal boundary conductance between the two layers. The heat flux boundary condition of the top, f_t , can be found with

$$f_t = \frac{A_0}{2\pi} \exp\left(-\frac{k^2 w_o^2}{8}\right) \quad (2.8)$$

which is the Hankel transform of a Gaussian spot with a power of A_0 and a $1/e^2$ radius of w_0 . If there are multiple layers, the solution can be found with

$$\begin{bmatrix} \theta_b \\ f_b \end{bmatrix} = \mathbf{M}_n \mathbf{M}_{n-1} \dots \mathbf{M}_2 \mathbf{M}_1 = \begin{bmatrix} A & B \\ C & D \end{bmatrix} \begin{bmatrix} \theta_t \\ f_t \end{bmatrix} \quad (2.9)$$

where \mathbf{M}_n is the matrix of the bottom layer. If the bottom layer is treated as adiabatic or semi-infinite, the surface temperature can be found using:

$$\theta_t = -\frac{D}{C} f_t \quad (2.10)$$

The final frequency response, $H(\omega)$, is found by taking the inverse Hankel transform of Eqn. 2.10 and weighting it with a Gaussian spot with a $1/e^2$ radius of w_1 :

$$H(\omega) = \frac{A_0}{2\pi} \int_0^\infty k \left(-\frac{D}{C}\right) \exp\left(-\frac{k^2(w_0^2 + w_1^2)}{8}\right) dk \quad (2.11)$$

The thermal model for $H(\omega)$ is then fitted to the lock-in phase data. By changing the parameters of the thermal model to fit the lock-in data, the thermal properties can be determined. The lock-in phase data measured is given by

$$\phi_{LI} = \tan^{-1} \frac{\Im(H(\omega))}{\Re(H(\omega))} + \phi_{ext} \quad (2.12)$$

where $\Im(H(\omega))$ is the out-of-phase signal, $\Re(H(\omega))$ is the reference signal, and ϕ_{ext} is the external phase shift caused by other aspects not caused by changes in reflectivity, such as the optical path length, driving electronics, and photodetectors.

In addition to the solution, phase sensitivity to a particular thermal property, x , at a given frequency can be found with

$$S(\omega) = \frac{\partial \phi(\omega)}{\partial \ln x} \quad (2.13)$$

Performing a sensitivity analysis allows us to understand which thermal properties can be determined from a frequency sweep. If the sensitivity to each of the thermal parameters varies differently along the frequency sweep, multiple thermal parameters can be determined from a single scan. If the sensitivities are near zero or the same between parameters, we cannot accurately determine those thermal properties.

2.3 System Validation with Reference Materials

The system was validated by measuring the thermal properties of well characterized materials as references. We used glass (SiO_2), sapphire (Al_2O_3), and silicon (Si) as our reference samples. The measured thermal conductivities of these three materials were compared to literature values, which can be seen below in Table 2.1. The thermal conductivity values for the three reference samples compared well with literature values, with the measured values falling well within 10% of the literature values.

The FDTR scans and sensitivity plots for glass, sapphire, and silicon used to extract the

Table 2.1: Measured thermal conductivity values of reference samples compared with literature.

Material	$\kappa [W m^{-1} K^{-1}]$		
	Measured	Literature Value	Citation
SiO ₂	1.29 ± 0.08	1.3	[22]
Al ₂ O ₃	34.8 ± 3.0	34	[23]
Si	138 ± 9.87	133	[23]

thermal conductivities are shown in Figure 2.4. The model was able to fit the data well, which gives us confidence with the code and system. Furthermore, each of the thermal properties had different sensitivities across the frequency spectrum, allowing for the determination of multiple thermal properties from a single sweep.

FDTR scans were also taken for sapphire in a cryostat to obtain thermal conductivity as a function of temperature, which is shown in Figure 2.5. The thermal conductivity as a function of temperature for the sapphire agreed well with literature values, giving us confidence in our temperature dependent measurements.

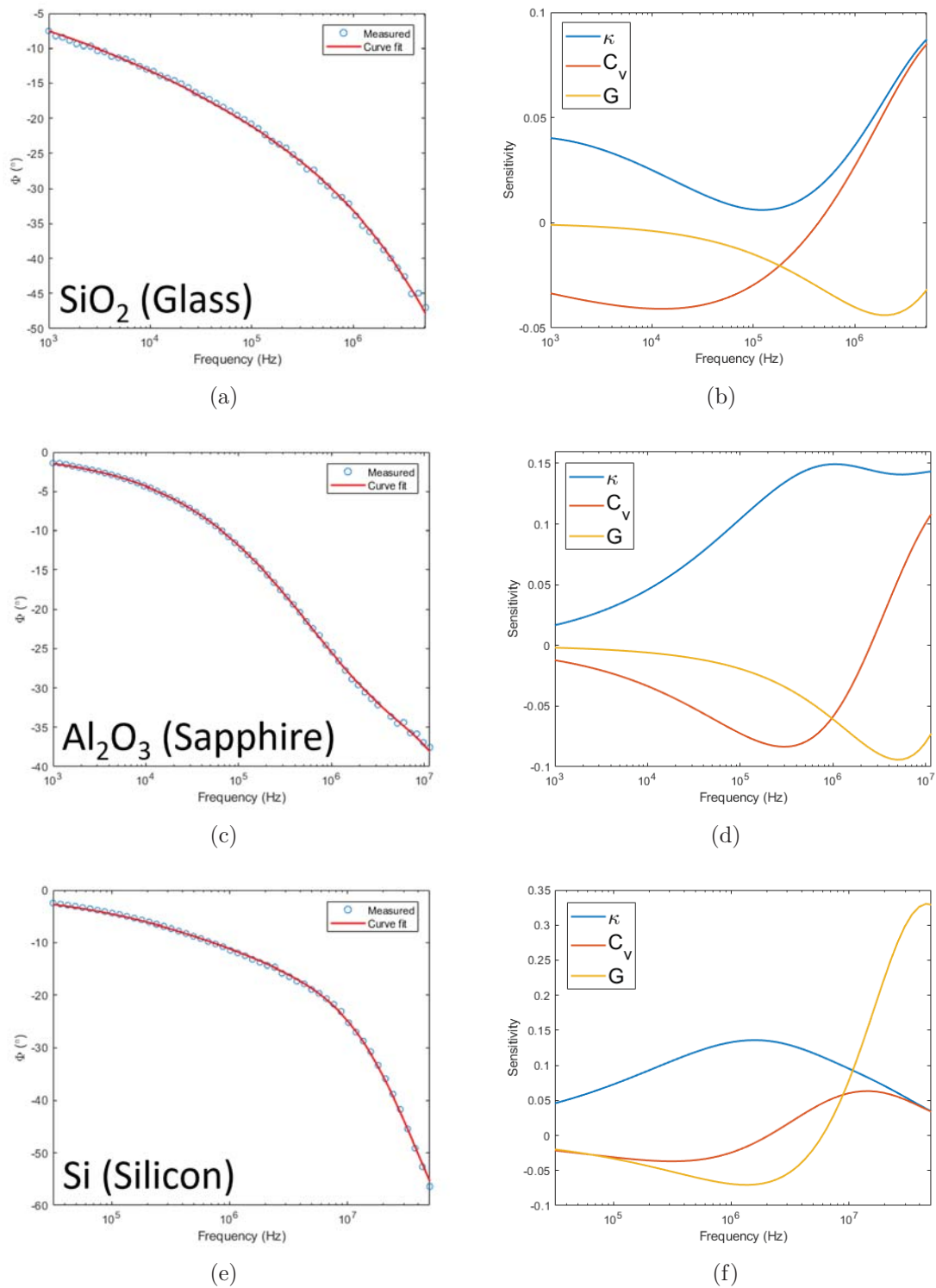


Figure 2.4: (a) FDTR solution for SiO_2 . (b) Sensitivity plot for SiO_2 . (c) FDTR solution for Al_2O_3 . (d) Sensitivity plot for Al_2O_3 . (e) FDTR solution for Si. (f) Sensitivity plot for Si.

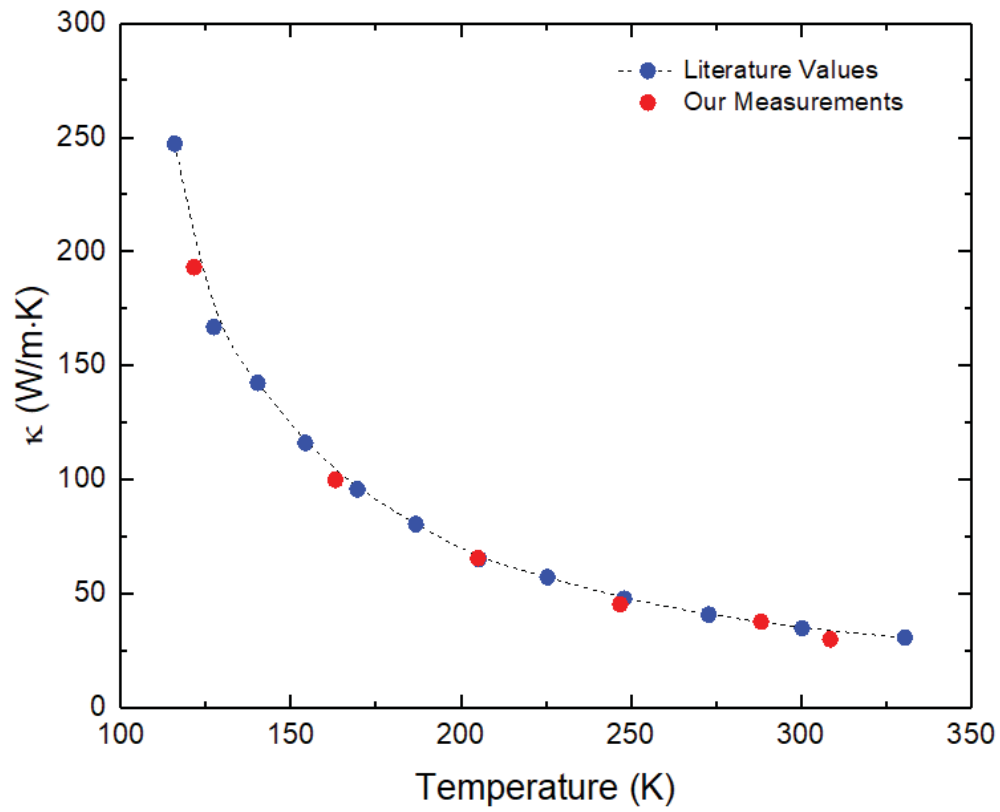


Figure 2.5: Measured thermal conductivity of sapphire as a function of temperature. These values are compared with values retrieved from Cahill [2].

3 Nickel Titanium Shape Memory Alloys

Shape memory alloys (SMAs) are materials that can recover their original shape after being deformed under certain conditions via the shape memory effect or super-elasticity [24]. The shape memory effect is a process where the material can recover its original shape by heating when deformed at a low temperature, while super-elasticity is a process where the material can recover its original shape by the removal of an applied load if deformed at a high temperature [24]. These properties are the result of the reversible, diffusionless solid-state phase transformation between austenite and martensite [24], [25]. Austenite is the parent phase stable at higher temperatures and smaller strains with a symmetrical crystal structure, while martensite is the phase stable at lower temperatures and higher strains with a less symmetrical crystal structure [25]. The austenitic-martensitic phase transformation can be induced by both temperature and strain [24].

The unique properties of SMAs have opened the door to a wide variety of applications, including those in medicine [26], [27], aerospace [28], and structural engineering [29]. One of the most promising applications of shape memory alloys is elastocaloric cooling, which has been identified as the non-vapor-compression technology with the highest potential to replace current vapor-compression systems [30]. Although vapor-compression systems have been the most widely used method for heating, ventilation, and air-conditioning, many of the refrigerants have negative environmental effects [30]. As a viable alternative, shape memory alloys can move heat using the latent heat of the austenitic-martensitic phase transformation, which is analogous to the liquid-vapor phase transformation in vapor-compression systems [31]. This can be seen in Figure 3.1. For elastocaloric cooling, the transformation from the austenitic to the martensitic phase is induced by the application of stress, causing entropy to decrease and latent heat to be released, while the transformation from the martensitic to the austenitic phase is induced upon the unload of stress, causing entropy to increase and heat to be absorbed from the environment [31].

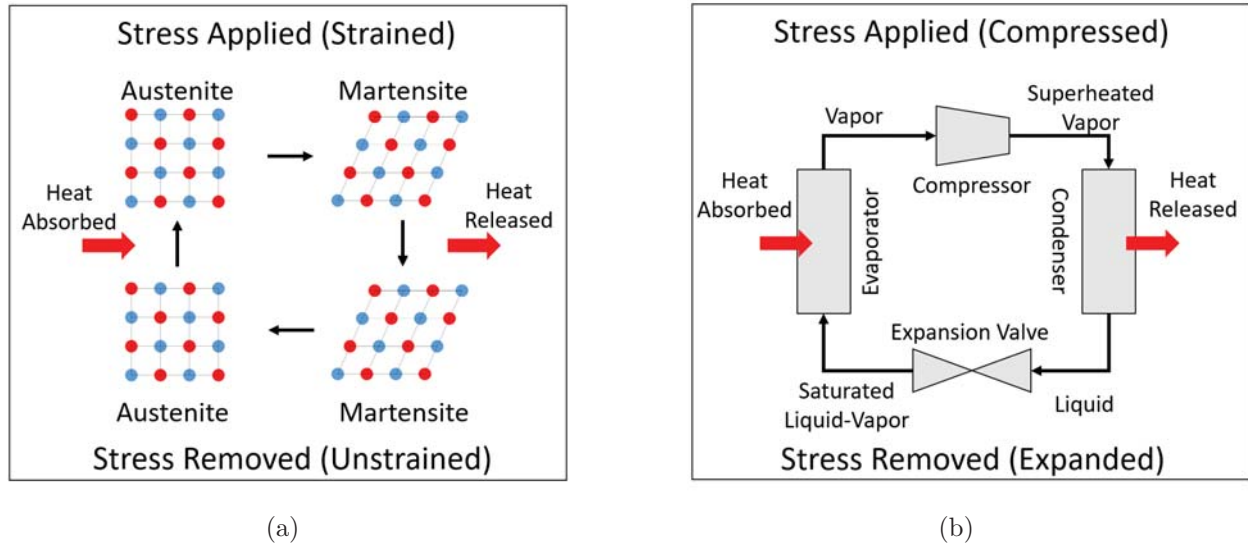


Figure 3.1: (a) Elastocaloric cooling cycle using the austenitic-martensitic phase transformation of SMAs. (b) A traditional vapor-compression refrigeration cycle. As shown from the two cycles, many of the principles are similar, such as the presence of two phases (solid-solid vs. liquid-vapor) and a form of stress applied (strain vs. compression).

The SMA that shows most promise for application is nickel-titanium, also known as NiTi or NITINOL. NiTi is the most popular SMA and was one of the first to be commercialized on a large scale [31]. Elastocaloric cooling devices with NiTi have one of the highest coefficient of performances (COPs) with predicted values as high as 11.8 [32]. Current studies have demonstrated COPs of 2.7 and 3.05 respectively for tension and compression of NiTi wires [32], 3.5 in a bending-mode elastocaloric cooling loop using NiTi wires [33], and 3.1 for a trained NiTi bridge-based elastocaloric cooling demonstrator [34]. NiTi also has one of the largest adiabatic temperature spans (ΔT_{ad}) of the most studied SMAs, which is an indicator of the latent heat and related to the mass-based energy density; from experiments, NiTi has a ΔT_{ad} ranging from 17-23 °C [31]. Another indicator of performance is the volumetric energy density, which NiTi also has one of the highest ranging from 60-82 MJ/m³ [31]. NiTi-based alloys are also unique in their low elastic anisotropy of around 2 (as opposed to 10 or more for other SMAs), the ability for amorphization to obtain smaller grain sizes, high ductility with the possibility for 60% cold working, and excellent resistance to corrosion and abrasion [35].

Measurement of the thermal properties of NiTi is important because it allows for the development of better models and understanding of its viability as a candidate material for elastocaloric cooling. For example, the thermal conductivity of the material is a critical property since it controls the rate at which heat can be added or removed from the system. The rate of heat transfer ultimately limits the frequency at which the cycle can be run and hence the cooling capacity of the material. However, the mechanisms that govern the thermal properties of NiTi are not well characterized. Some studies have shown significant differences in thermal conductivity between martensite and austenite, but the results have not been consistent. A summary of results can be seen below in Table 3.1.

Table 3.1: Measured thermal conductivities of NiTi and associated temperature range.

Reference	κ [$W\ m^{-1}K^{-1}$]	Measurement Method	Temperature Range
Terada et al. [36]	15	Laser Flash	300 K
Rohde and Schüßler [37]	17-22	Laser Flash	300-400 K
Faulkner et al. [38]	14 (M), 28 (A)	Electro-thermal	<340 K (M), >345 K (A)
Jain and Goodson [39]	8.9-13.7	3- ω	323 K - 573 K
Zannotti et al. [40]	9-13	Steady State Heat Meter Bar	290 K - 520 K

Due to the difference between the thermal conductivity of martensite and austenite phases, a better understanding of the thermal properties can be gained by analyzing the material as a function of temperature. Furthermore, one factor that may have affected thermal conductivity is the grain size, which has been shown to dramatically affect the martensitic phase transformation [41]. For NiTi, Ahadi and Sun have shown that grain sizes below 60 nm have a dramatic decrease in the hysteresis loop area and temperature dependence of transition stress [41]. Furthermore, smaller grain sizes have smaller temperature oscillation amplitudes, have smaller specific latent heats, and require more stress to achieve phase transformation [41]. Because of these effects of grain size, a study of grain size on the thermal properties is also important in the characterization of NiTi.

Using FDTR, the goal of the project is to determine the thermal conductivity of NiTi of different grain sizes as a function of temperature at both sides of the phase transition.

3.1 Fabrication and Microscopy

The 50-50 NiTi samples were purchased from a commercial vendor and cut into ribbons. The grains were grown through a solution anneal in a furnace above 800 °C, which is above the reported 630 °C solid solution temperature [42]. This temperature was used to prevent Ni_4Ti_3 precipitate growth, which is common in Ni-rich, low temperature heat treatment. Two heat treatment times of 3 min and 5 min were performed. After heating in the furnace, the samples were quenched in a water bath. Because the furnace was open to the atmosphere, oxidation occurred on the samples, which was removed by ion milling using a GatanTM PIPS II system to polish the samples prior to TEM/SEM imaging and the application of the transducer.

Transmission electron microscopy (TEM) and scanning electron microscopy (SEM) were used to image the materials and determine the average grain size ($\langle d \rangle$) and grain orientation. The TEM characterization was performed using a JEOLARM200F TEM operated at 200 keV. The SEM characterization was performed using an FEI NanoSEM. The TEM images of the "As-Received" nanograined samples are shown in Figure 3.2.

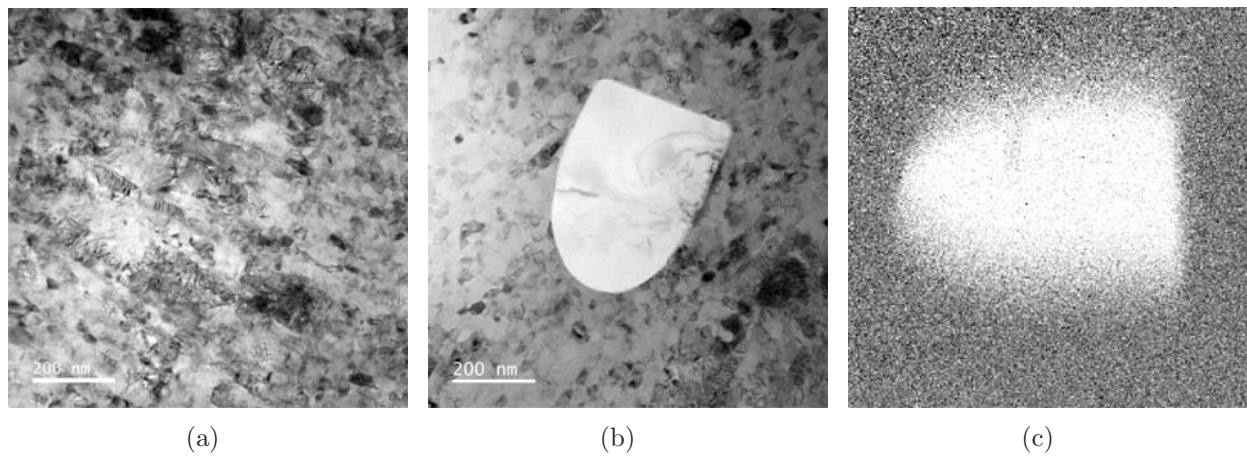


Figure 3.2: TE bright field TEM micrograph of AR specimen showing: (a) representative region of NiTi microstructure, (b) large, single crystal Ti inclusion, and (c) %Ti EDS map of Ti inclusion, where white is 100%, suggesting that the inclusions were pure Ti.

Determined from the TEM, the $\langle d \rangle$ was 40 ± 30 nm, and the grains were largely

equiaxed with some elongation along the long axis of the ribbon. These nanosized grains likely resulted in increased grain boundary scattering of the energy carriers, causing a lower thermal conductivity on both sides of the phase transition. Also shown in the TEM were some $0.5\text{-}2\ \mu\text{m}$ secondary phase particles of pure Ti, as determined from energy-dispersive X-ray spectroscopy (EDS). The particles were likely formed during the melt because they are far from the equilibrium phase during heat treatment. These Ti particles are expected to also cause a decrease in thermal conductivity due to defect scattering. However, the particles were sparse and remained throughout the annealing process.

For the annealed samples, electron backscatter detection (EBSD) was used to determine the grain size and orientation. The $[001]$ inverse pole map obtained from EBSD for the 3 min annealed sample is shown in Figure 3.3.

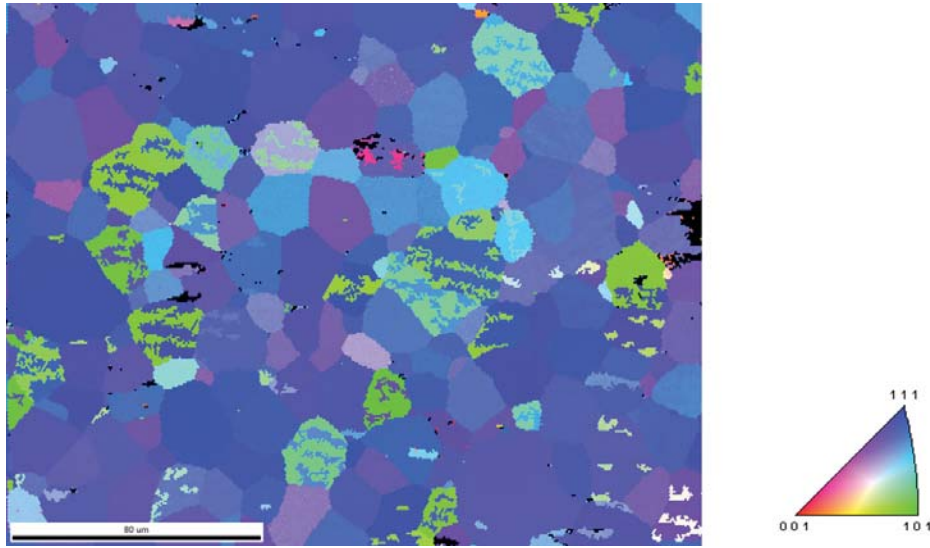


Figure 3.3: $[001]$ inverse pole map obtained from EBSD of 3 min annealed sample, which determined grain size to be $39 \pm 10\ \mu\text{m}$ and showed textured B2 austenite and R-phase' martensite.

The inverse pole map showed a mixture of heavily textured B2 austenite (as shown from the grains with a single color) and R-phase' martensite (as shown from the grains with multiple colors). The EBSD also determined that the $\langle d \rangle$ of the the 3 min annealed sample was $39 \pm 10\ \mu\text{m}$.

The TEMs of an R-phased grain of the 3 min sample is shown below in Figure 3.4.

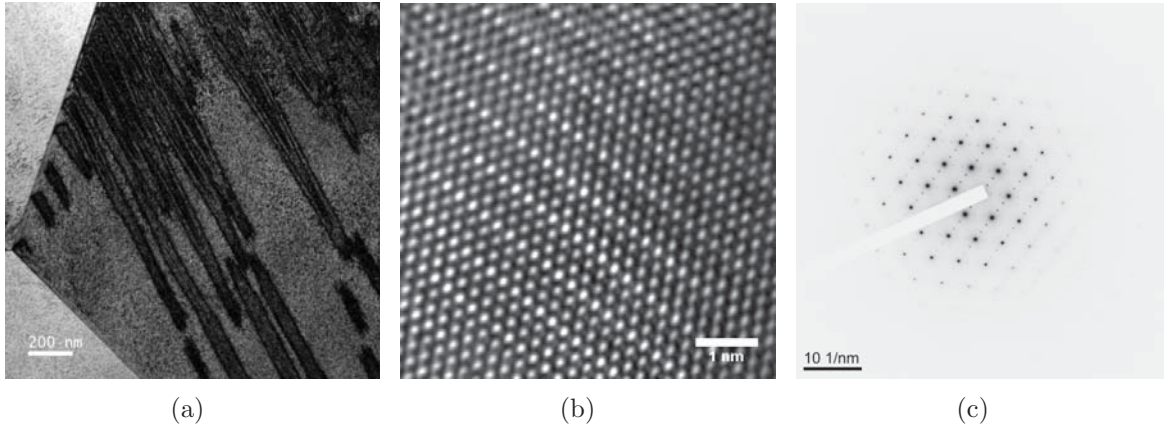


Figure 3.4: (a) Bright field TEM micrograph showing R-Phase grain adjacent to two B2 Austenite grains. (b) Absolute background filtered HRTEM micrograph from the same R-phase grain. The image shows a 0.635 nm periodic spacing between $[10\bar{1}0]$ planes. (c) $[\bar{2}01]$ zone axis selected area diffraction pattern for same R-phase grain.

The $[001]$ inverse pole image obtained of the 5 min samples from EBSD is shown in Figure 3.5. The inverse pole map of the 5 min annealed sample had similar grain orientations as the 3 min annealed sample. The $\langle d \rangle$ of the the 5 min annealed sample was $56 \pm 13 \mu\text{m}$. The TEM images of B2 austenite grains of the 5 min annealed sample is shown in Figure 3.6.

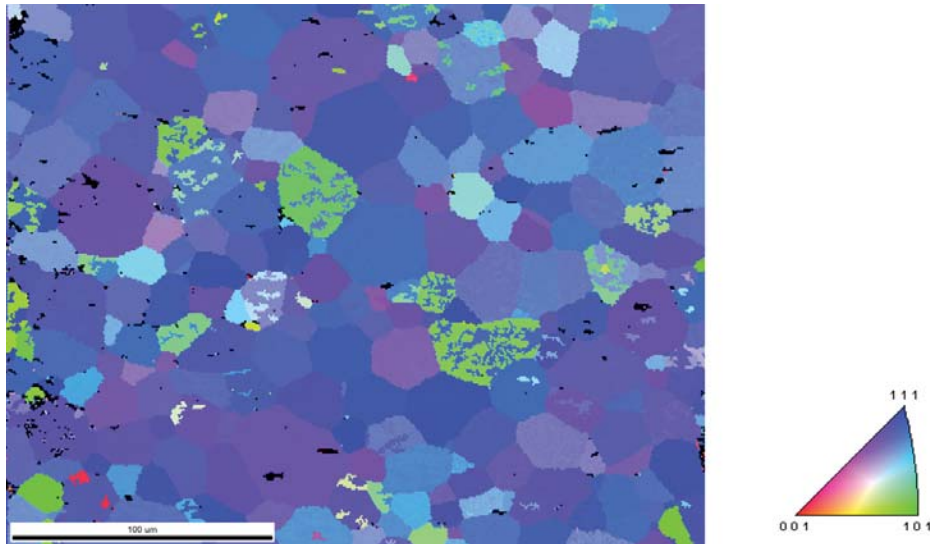


Figure 3.5: $[001]$ inverse pole map obtained from EBSD of 5 min annealed sample, which determined grain size to be $56 \pm 13 \mu\text{m}$ and showed textured B2 austenite and R-phase' martensite.

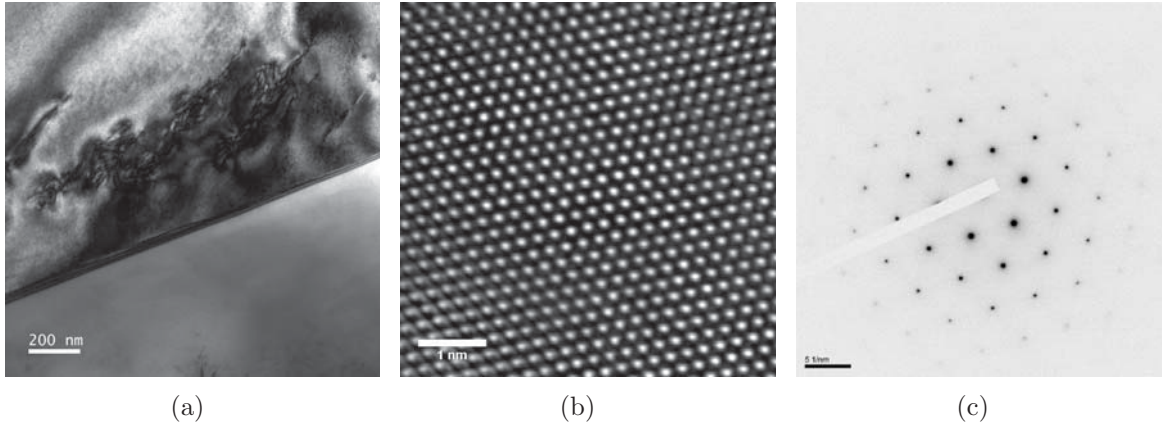


Figure 3.6: (a) Bright field TEM micrograph showing the interface between two B2 Austenite grains. (b) Absolute background filtered HRTEM micrograph from the upper grain in (a). (c) [111] zone axis selected area diffraction pattern for same R-phase grain.

3.2 Results and Analysis

The thermal conductivity, heat capacity, and thermal boundary conductance were measured by FDTR. The phase lag at the transducer surface was measured within the frequency range of 40 kHz to MHz. An example of a frequency sweep and sensitivity plot are shown in Figure 3.7 for a 30 s annealed sample.

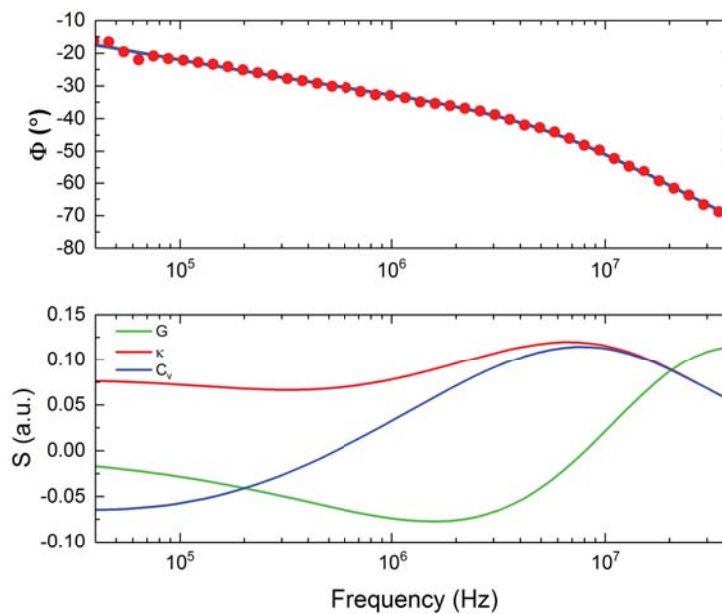


Figure 3.7: Example FDTR result and sensitivity plot of a 30s annealed sample.

The thermal conductivity of the three samples (as-received, 3 min annealed, and 5 min annealed) were measured as a function of temperature above and below the transition temperature. The results are shown in Figure 3.8.

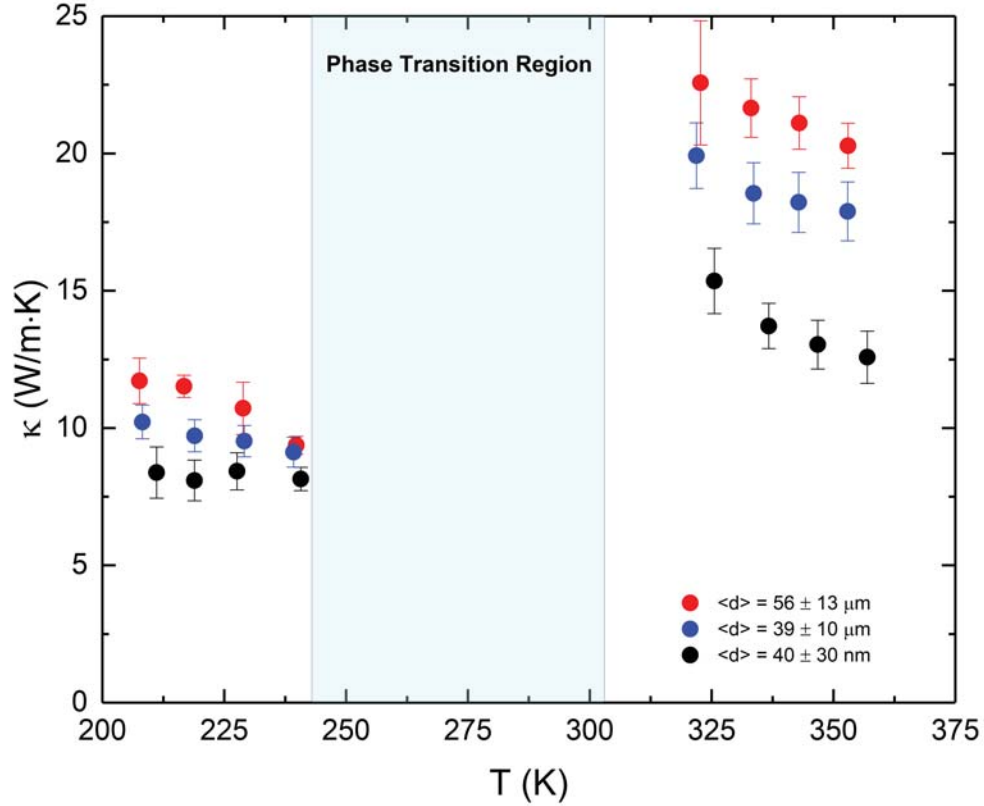


Figure 3.8: Thermal conductivity as a function of temperature for the nanograind as-received sample ($\langle d \rangle = 40 \pm 30 \text{ nm}$), the 3 min annealed sample ($\langle d \rangle = 39 \pm 10 \mu\text{m}$), and the 5 min annealed sample ($\langle d \rangle = 56 \pm 13 \mu\text{m}$).

First, there was a clear difference in thermal conductivity in the martensite and austenite phase, with the martensite phase having a larger thermal conductivity. This is consistent with what was found in literature [38–40]. More importantly, we saw a significant increase in thermal conductivity on both sides of the phase transition with an increase in grain size. The 5 min annealed sample saw up to a $\sim 1.5x$ improvement with κ .

Another observation was that in the martensite phase, the annealed samples showed a

$1/T$ relationship for thermal conductivity, while the nano-grained samples saw a relatively constant thermal conductivity. The $1/T$ result seen in the annealed samples is consistent with materials whose thermal transport is dominated by electron mobility. Meanwhile, the nano-grained samples likely faced increased grain boundary scattering. This ability to tailor a material's thermal conductivity opens a wide parameter space for engineers to use. Nonetheless, we suggest that additional samples be tested to determine the limits to improvement as well as the minimum grain size before grain boundary scattering becomes the dominant scattering mechanism.

3.3 Conclusions

Using FDTR, the thermal properties of a nano-grained as-recieved sample, 3 min annealed sample, and 5 min annealed sample of NiTi was measured. The results saw an increase in thermal conductivity between the martensite and austenite phase consistent with literature. Moreover, the results saw the thermal conductivity increase with an increase in grain size. The results for the nano-grained NiTi were in line with what is expected by a system dominated by grain boundary scattering. These results suggest that the thermal properties of NiTi can be tailored to meet different needs by altering the grain size.

4 Germanium Telluride

Germanium Telluride (GeTe) is a chalcogenide glass phase change material, and these materials have the ability to reversibly change states between an amorphous (a-GeTe) and a crystalline (c-GeTe) phase. These two discrete states have significantly different properties, which have opened the door to a wide variety of applications. The low reflectivity of the amorphous phase, high reflectivity of the crystalline phase, and ability to quickly change phase with rapid laser pulses has led to advances in many optical applications, primarily optical data storage in the form of rewriteable disks (i.e. compact disks, digital versatile disks, and Blu-Ray) [7, 43] and more recently, photonic memory chips [8]. The area GeTe has gained the most attention for is in its electrical applications such as a potential material for non-volatile memory and radiofrequency (RF) switching due to its insulating amorphous phase, conducting crystalline phase, high memory density, and ability to undergo nanosecond switching upon the application of voltage or heat [6, 44–48].

Although the electronic transport properties of GeTe have been explored in depth, the knowledge on the thermal transport in GeTe thin films is immature. The majority of the studies on the thermal conductivity of GeTe focused on the bulk properties of c-GeTe [46, 49–51]. However, we believe that the length scale of the material could have a significant impact on the thermal transport, especially as technologies push towards length scales that approach the mean free path of the energy carriers. At these length scales, traditional macroscale heat transfer principles based on thickness, such as the diffusive nature of heat flow in Fourier’s law, break down as additional scattering mechanisms have a significant impact on the thermal conductivity [52–54]. For example, thermal conductivity of thin silicon films has been shown to be much lower than bulk values due to phonon boundary scattering [55].

Three papers do explore the nanoscale effects on thin films of crystalline and amorphous GeTe. Nath and Chopra found a significant difference in the thermal conductivities between the amorphous and crystalline phases, although they did not find a thickness dependence on

thermal conductivity [56]. They attribute this to a small phonon mean free path of 0.5 nm for a-GeTe and 2 nm for c-GeTe. However, Nath and Chopra only studied films as small as 200 nm and found thermal conductivity with a thermal gradient over a multiple cm length scale. Bosse et al. also observed a significant difference in thermal conductivity between amorphous and crystalline GeTe [57]. However, the study only studied film sizes of 100 nm and 200 nm and did not attempt to find a length-scale effect of thermal conductivity, although they assumed that the mean free path was smaller than the characteristic lengths in order to use a diffusive heat transfer equation and a uniform thermal boundary conductance between the two films to extract the thermal properties. Fallica et al. studied length scales similar to our study, exploring film thicknesses as low as 30 nm [58]. However, their work relied on characterization via $3-\omega$, which forces the use of thickness-independence of total thermal resistance between the heat source and back side to extract a thermal boundary resistance between the heater and film, thereby negating the ability to understand the impacts that reductions in film thickness have on the thermal properties of GeTe.

Using FDTR, we characterize the thermal properties of amorphous and crystalline GeTe with thickness spanning from 30 nm to 1.2 μm . By using FDTR, the thermal boundary conductance between an upper transducer layer and the sample can be found independently from the thermal conductivity. This technique as well as the smaller film thicknesses allow us to gain a better understanding of the length scale effects on the thermal transport of amorphous and crystalline phases of GeTe and other similar binary alloys using a Debye, or "Characteristic" intrinsic mean free path.

4.1 Material Synthesis and Physical Characterization

The GeTe thin films of varying target thicknesses (30 nm, 100 nm, 700 nm, and 1200 nm) were deposited onto c-plane sapphire substrates via magnetron sputtering of a compound target (Ge:Te=1:1). Sputtering took place at room temperature in a 5 mTorr Ar atmosphere and resulted in amorphous GeTe films with a composition of 51% Ge and 49% Te based on x-ray

photoelectron spectroscopy (XPS). C-GeTe films were achieved by annealing amorphous as-deposited samples for 250 °C for 10 minutes in an Ar atmosphere. The phase transition was confirmed by the increased optical reflectivity and electrical conductivity of the crystallized films.

Actual film thicknesses and densities of the 30 nm and 100 nm films were measured by x-ray reflectivity (XRR) with an expected error of less than 1%, while the thicknesses of the 700 nm and 1200 nm films were measured using profilometry with an expected error of less than 3%. These thicknesses are shown in Table 4.1. Due to the density increase that accompanies crystallization, crystalline GeTe films of a particular target thickness were 11-13% thinner than the corresponding amorphous GeTe films.

Table 4.1: GeTe target and measured film thicknesses.

Target Thickness [nm]	a-GeTe [nm]	c-GeTe [nm]
30	37.0	32.8
100	104.9	92.1
700	700.	623
1200	1270.	1105

The samples were then coated with a transducer to take the FDTR data. This layer consisted of a 2 nm Ti adhesion layer and an 80 nm Au reflective layer deposited using e-beam evaporation in a high vacuum ($< 10^{-6}$ Torr), with metal film thickness confirmed via profilometry.

4.2 Results and Discussion

Figure 4.1 shows the FDTR scans curve fit for the thickest amorphous and crystalline samples. Figure 4.1 also shows the sensitivity to the thermal properties for the thickest c-GeTe samples. The sensitivity plot shows that each of the thermal properties are sensitive at distinct frequencies across the sweep from 4 kHz to 20 MHz.

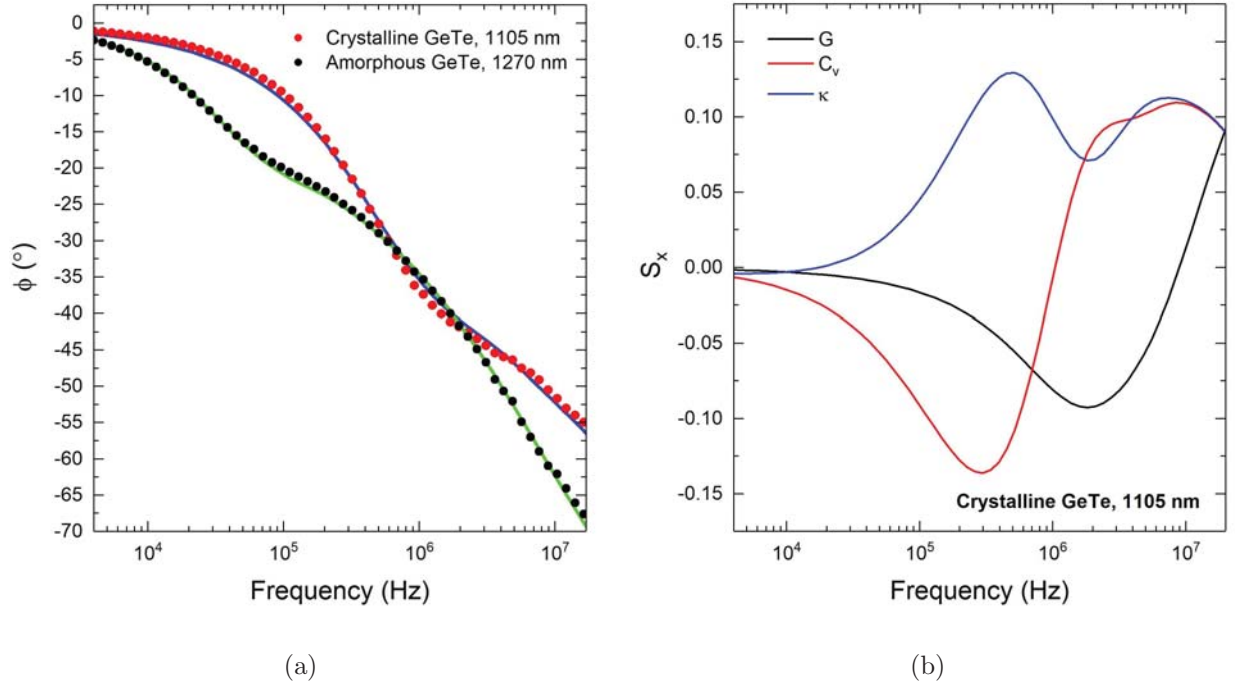


Figure 4.1: (a) FDTR scans and curve fits for thickest c-GeTe and a-GeTe samples. (b) Sensitivity plot of the thickest c-GeTe sample.

Figure 4.2 shows the thickness dependence of both the amorphous and crystalline GeTe films. First, the results show a clear difference in the thermal conductivities between a-GeTe and c-GeTe. The results show a clear decrease in thermal conductivity with films nominally 100 nm thick and below, with observed reductions of up to 80% compared to the nominally 700 nm and 1200 nm thick films. This thickness dependence is typical of materials systems with thermal transport dominated by thermal carrier boundary scattering. This implies that the vibrational mean free paths in both phases are greater than the film thicknesses measured. Moreover, both the amorphous and crystalline systems exhibited similar trends in thermal conductivity, suggesting a similar mean free path. These results are interesting because the mean free path is typically limited by alloy or impurity scattering in a binary alloy. Moreover, the mean free path of amorphous systems is expected to further be impacted by the lack of long range atomic order.

These results can be fit with a vibrational thermal transport model that recasts the thermal carriers into a Kinetic Theory of Gasses framework. The thermal conductivity, κ ,

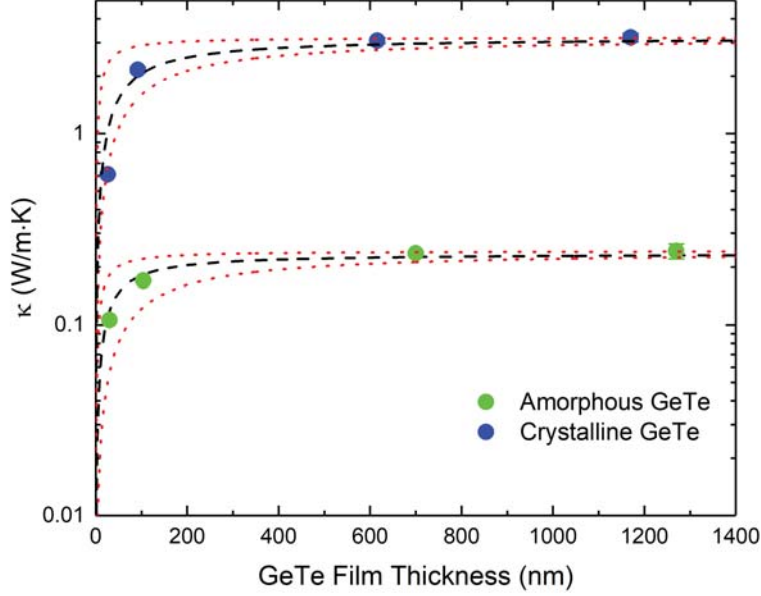


Figure 4.2: κ as a function of film thickness for c-GeTe and a-GeTe.

of the film can therefore be approximated with

$$\kappa = \frac{1}{3} C_v v \Lambda \quad (4.1)$$

where C_v is the volumetric heat capacity, v is the vibrational carrier speed, and Λ is the mean free path of the vibrational carriers. For this simple model, mean free path of the vibrational carriers can be treated as a combination of the intrinsic mean free path, Λ_{in} , and the mean free path imposed by film thickness, Λ_{film} . These can be combined using Mathiessenn's rule:

$$\frac{1}{\Lambda} = \frac{1}{\Lambda_{in}} + \frac{1}{\Lambda_{film}} \quad (4.2)$$

We assume that the mean free path imposed by boundary scattering is equal to the thickness of the film itself. Furthermore, we assume that the heat capacity, vibrational carrier speed, and intrinsic mean free path are all constant for a given phase of GeTe. This allows us to fit

a model where the only free parameter is the mean free path of the vibrational carriers due to boundary scattering. This reduces the mean free path spectrum of vibrational carriers down to one characteristic mean free path, which although leaves an incomplete picture of the vibrational spectrum, provides valuable insight with a minimum number of assumptions.

The intrinsic mean free path was extracted by normalizing the thermal conductivity to the thickest films, which is insensitive to boundary scattering:

$$\kappa(\Lambda_{film}) = \kappa_{bulk} \frac{\Lambda}{\Lambda_{bulk}} = \kappa_{bulk} \frac{1}{1 + \Lambda_{in}/\Lambda_{film}} \quad (4.3)$$

With the assumptions made, the only unknown variable is the intrinsic characteristic mean free path of the material, Λ_{in} . By fitting this equation with the measured thermal conductivities, we found that Λ_{in} was 63 nm for c-GeTe and 45 nm for a-GeTe, and these are plotted as the black dotted lines in Figure 4.2. Also shown as the red dotted lines are the characteristic mean free paths of 100 nm and 10 nm to demonstrate the sensitivity of the model, and the results clearly fit within this range. The characteristic mean free paths of a-GeTe and c-GeTe demonstrate similar thermal carrier scattering mechanisms despite having a phonons transporting heat in c-GeTe and propagons and diffusions carrying heat in a-GeTe. This result suggests a similarity between phonon transport and propagon/diffusion transport and serves to emphasize the need for the development of a theoretical understanding of amorphous heat carriers.

4.3 Conclusions

The thermal conductivity of c-GeTe and a-GeTe thin films with nominal thicknesses ranging from 30 to 1200 nm were measured. We found that c-GeTe had a higher thermal conductivity than a-GeTe. Furthermore, we saw a decrease in thermal conductivity with a decrease in grain size consistent with boundary scattering. By using a Kinetic Theory of Gasses framework and normalizing to the bulk samples, we found that the intrinsic mean free

path was 63 nm for c-GeTe and 45 nm for a-GeTe, suggesting similar scattering transport mechanisms despite differences in structure and energy carriers. More studies should be performed for a fundamental understanding of amorphous heat carriers.

5 $\text{Bi}_2\text{Te}_3/\text{Bi}_2(\text{TeSe})_3$ Superlattices

This work explores the anisotropic thermal properties of superlattices with alternating thin layers of Bismuth Telluride (Bi_2Te_3) and $\text{Bi}_2(\text{TeSe})_3$. By doing so, we explore the unique physics of topological insulators, thermoelectrics, and superlattices, which have drastically different effects on—or have performance drastically affected by—the in-plane and through-plane thermal conductivity.

Topological insulators are a unique subset of materials that insulate on the interior but conduct like a metal on the surface [10, 59, 60]. Topological insulators are unique because they have they appear to exhibit characteristics similar to the quantum Hall effect without the need for extreme temperature or magnetic fields, and this effect could potentially be used in a 3D material [59, 61]. These materials could lead to breakthroughs in spintronic devices, magnetoelectric devices, and new types of quantum computers [59]. One of the most promising topological insulator for these applications is Bi_2Te_3 , a second generation 3D topological insulator that has been experimentally proven and one that could potentially exhibit quantum Hall behavior at room temperature [10, 60, 62, 63].

Topological insulators also have unique thermal properties that could be exploited for other novel applications. For one, most topological insulators are excellent candidate materials for thermoelectrics [64, 65], which are materials that can convert heat directly into electricity due to the Seebeck effect [9]. In fact, Bi_2Te_3 is the most widely used commercial thermoelectric material, and it and its alloys has some of the highest dimensionless thermoelectric figure of merits [9, 66, 67]. This dimensionless figure of merit is the primary measure of a thermoelectric performance, and it is shown in Equation 5.1 [9].

$$ZT = S^2\sigma T/\kappa \quad (5.1)$$

where Z is the thermoelectric figure of merit, T is the absolute temperature, S is the Seebeck coefficient, σ is the electrical conductivity, and κ is the thermal conductivity. As shown

from this equation, a high Seebeck coefficient, high electrical conductivity, and low thermal conductivity increases the effectiveness of the thermoelectrics. This is what makes topological insulators effective for this application, as the electronic contribution of the topologically protected boundary state can be tuned with respect to the phonon contribution by changing the geometric size, which introduces additional scattering mechanisms with the addition of disorders and defects [65].

One common manufacturing technique used to increase thermoelectric performance is incorporating the material into a superlattice, which is the repeated layering of two or more materials with period thicknesses on the order of one nanometer. Superlattices have been shown to increase ZT to as high as 2.4 for $\text{Bi}_2\text{Te}_3/\text{Sb}_2\text{Te}_3$ superlattices at room temperature due to phonon blocking and electron transmission [68]. Furthermore, superlattices have been attributed to high anisotropy in electrical and thermal conductivity due to an increase in boundary scattering across the layers [69]. The increase in anisotropy becomes more significant in Bi_2Te_3 because it is already anisotropic in bulk form [70–72].

Altering the thicknesses of topological insulators have also caused interesting observations. For example, Luo et al. has shown that altering the thin films of $\text{Bi}_2\text{Te}_2\text{Se}$, a topological insulator, below 20 nm has been able to dramatically increase thermal and electrical conductivity as well as Lorenz number due to the activation of the topological insulator effect [73]. If we activate the topological insulator effect in our materials, we could potentially see increases in anisotropy or even thermal conductivity due to electron thermal transport on the surfaces. By combining the unique properties of topological insulators and thermoelectrics, the inherent anisotropy of Bi_2Te_3 , and the increase in anisotropy from thin films and superlattices, $\text{Bi}_2\text{Te}_3/\text{Bi}_2(\text{TeSe})_3$ superlattices have the potential for high thermal anisotropy and strange thermal physics.

5.1 Sample Set and Microscopy

Three samples of $\text{Bi}_2\text{Te}_3/\text{Bi}_2(\text{TeSe})_3$ superlattices were studied. These samples were fabricated on a 140 nm layer of pure Bi_2Te_3 over a GaAs substrate. The samples had repeated periods of 1 nm Bi_2Te_3 and either 5 nm, or 6 nm $\text{Bi}_2(\text{TeSe})_3$. The samples were then coated with an 80 nm Al transducer.

A diagram of the superlattices is shown in Figure 5.1, and an overview of the materials studied is shown in Table 5.1, where $t_{\text{Bi}_2\text{Te}_3}$ is the period thickness of Bi_2Te_3 , $t_{\text{Bi}_2(\text{TeSe})_3}$ is the period thickness of $\text{Bi}_2(\text{TeSe})_3$, n is the number of periods, and t_{tot} is the total thickness.

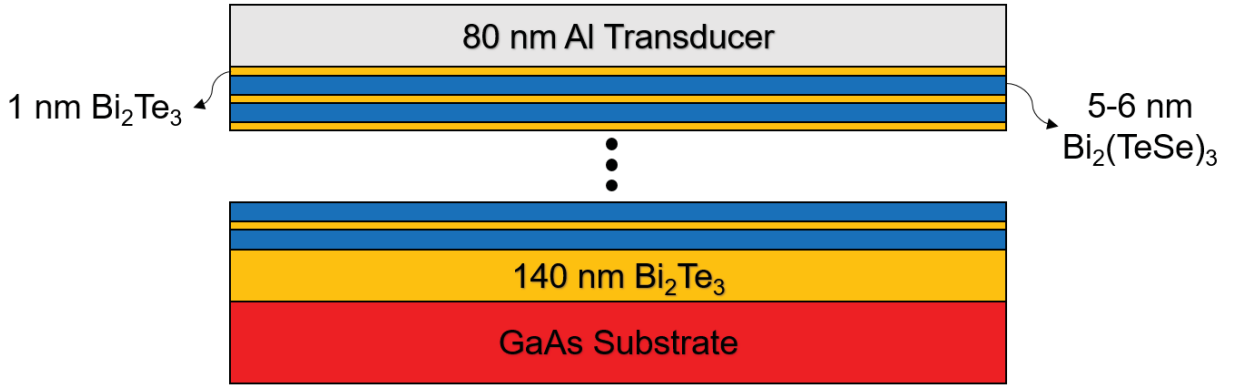


Figure 5.1: Diagram of Superlattice Material Stack.

Table 5.1: Overview of the three $\text{Bi}_2\text{Te}_3/\text{Bi}_2(\text{TeSe})_3$ superlattices configurations studied.

$t_{\text{Bi}_2\text{Te}_3}$ [nm]	$t_{\text{Bi}_2(\text{TeSe})_3}$ [nm]	n	t_{tot} [μm]
1	5	167	1.14
1	5	190	1.28
1	6	50	0.49

TEMs of the interface between the superlattice and Bi_2Te_3 buffer as well as the TEM of the interface between the Bi_2Te_3 buffer and GaAs substrate are shown in Figure 5.2. The TEMs show a significant amount of dislocations between the layers, which could indicate diffusion between layers. This is a possibility due to the similar chemical composition of the constituent layers, and this would cause $\text{Bi}_2(\text{TeSe})_3$ to diffuse downward to the Bi_2Te_3 layer underneath. This could potentially mean that the superlattice acts as a bulk material

instead with a 1nm thin layer of Bi_2Te_3 on top. This may explain some of the interesting results we got, which will be discussed in the next section.

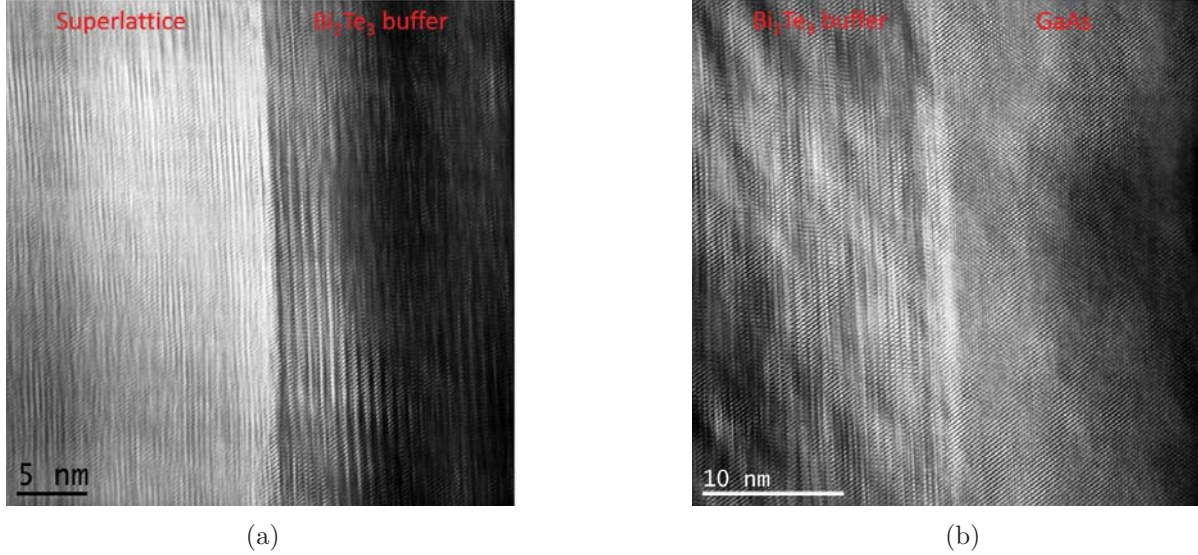


Figure 5.2: (a) HRTEM of the interface between the superlattice and Bi_2Te_3 buffer. (b) HRTEM of the interface between the Bi_2Te_3 buffer and GaAs substrate.

5.2 Results and Discussion

In-plane and cross-plane thermal conductivity (κ_{\parallel} and κ_{\perp}) measurements of the samples were taken with FDTR using 808 nm (red) as the probe and 532 nm (blue) for the pump. Electrical resistivity (ρ) measurements were taken using 4-point probe. The results are shown in Table 5.2.

Table 5.2: In-plane and cross-plane thermal conductivity and electrical resistivity of the $\text{Bi}_2\text{Te}_3/\text{Bi}_2(\text{TeSe})_3$ superlattice configurations studied. The anisotropy ratios and effective Lorenz numbers were also calculated.

$t_{\text{Bi}_2\text{Te}_3}$ [nm]	n	t_{tot} [μm]	κ_{\perp} [$\text{W m}^{-1}\text{K}^{-1}$]	κ_{\parallel} [$\text{W m}^{-1}\text{K}^{-1}$]	ρ [$\Omega \text{ cm}$]	$\kappa_{\parallel}/\kappa_{\perp}$	L [$\text{W}\Omega\text{K}^{-2}$]
5	190	1.28	0.85 ± 0.07	6.5 ± 0.32	0.00459	7.6	7.96×10^{-7}
5	167	1.14	0.9 ± 0.08	9.2 ± 0.43	0.00345	10.2	6.36×10^{-7}
6	50	0.49	0.87 ± 0.09	17 ± 0.66	0.00289	19.6	1.43×10^{-6}

As shown here, we found a large increase in the in-plane thermal conductivity as well as

significant anisotropy when compared with published bulk and thin film values. Meanwhile, the cross-plane thermal conductivity aligned with literature values for thin films. The thermal conductivity of Bi_2Te_3 has been reported by Goldsmid to be $1.9\text{--}2.4 \text{ W m}^{-1}\text{K}^{-1}$ [74], while Pettes found thermal conductivity to range from $0.9 \text{ W m}^{-1}\text{K}^{-1}$ for a 9.2 nm sample and $2.8 \text{ W m}^{-1}\text{K}^{-1}$ for a 25.2 nm sample [75]. We also found a general downward trend with the in-plane thermal conductivity with an increase in electrical receptivity, which is shown in Figure 5.3. Although there was also a trend with the number of periods (lower conductivity with more periods), we are hesitant to make this connection due to the potential mixing observed between the layers.

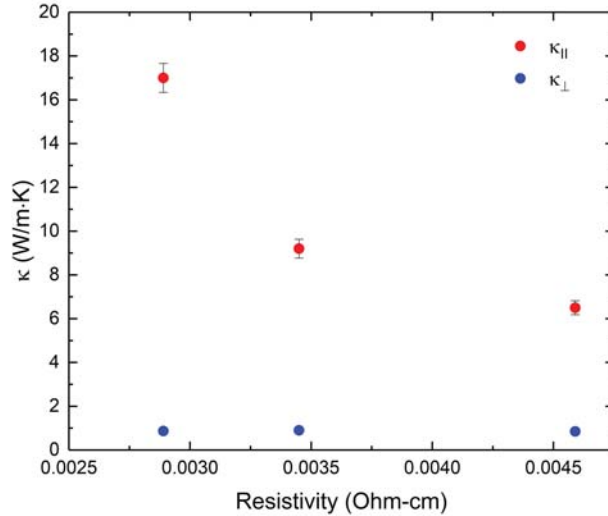


Figure 5.3: In-plane and cross-plane thermal conductivity of $\text{Bi}_2\text{Te}_3/\text{Bi}_2(\text{TeSe})_3$ as a function of electrical resistance.

By comparing the value of thermal conductivity to electrical resistivity, we can make hypotheses about the electron contribution to thermal conductivity. We believe that we are activating the topological insulator effect, opening up additional channels for thermal transport. A similar effect to a lesser extent was observed Luo et al, who saw both the thermal conductivity increase up to 2.8 times bulk values and predicted a possible tenfold increase in Lorenz number as the film thickness of topological insulators decreases [73]. We saw approximately a seven times improvement from bulk values and an approximately 60

times improvement in a calculated effective Lorenz number, which used the Wiedemann-Franz Law, sheet resistance, and an effective electrical contribution to thermal conductivity determined by subtracting the bulk values from the in-plane thermal conductivity.

If the mixing was significant enough, we could effectively have a 1 nm thin film layer of Bi_2Te_3 with activated over a bulk structure. The decrease in thermal conductivity with increased resistivity could correspond to depleted energy carriers on the surface.

In order to gain a better understanding of our observations, we intend to take Hall measurements, sheet resistance measurements, and additional thermal conductivity measurements, all as a function of temperature. Furthermore, we intend to measure the thermal conductivity with a special built FDTR system that uses elliptical spot sizes, which makes the measurements more sensitive to anisotropy. These would allow us to see if we are depleting the energy carriers and validate the ultra-high anisotropy observed.

5.3 Conclusions

$\text{Bi}_2\text{Te}_3/\text{Bi}_2(\text{TeSe})_3$ Superlattices were studied, and we found a large increase in the in-plane thermal conductivity (an approximate sevenfold increase compared to bulk), a large amount of anisotropy (a maximum anisotropy ratio of 19.6 observed), and a large increase in the Lorenz number (an approximately 60 fold increase compared to the Sommerfeld value). We believe that this may have been caused by the activation of additional transport mechanisms due to the topological insulator effect, which has been observed in similar thin films. For a better understanding, Hall measurements, sheet resistance measurements, and thermal conductivity measurements will be taken as a function of temperature to better understand the observed phenomenon.

6 Gallium Nitride

Power electronics, which are devices that control the flow of electrical energy for energy conversion, have been the center the technological advances in system controls, power and energy management, and electronic devices [11]. The backbone to power electronics are semiconductors for the use as switches and rectifiers, and the predominant material used for these applications has been silicon [11].

Gallium nitride (GaN) based devices have seen a surge in research interest and commercial application in the past two decades due to a tenfold increase in power density, high voltage capability, improved efficiency, improved reliability, smaller size, and superior performance over existing technologies [11, 76, 77]. Much of the improvement is attributed to the wide bandgap and extremely high electron concentration in GaN based devices, specifically with two-dimensional electron gas (2DEG) AlGa_N/Ga_N high electron mobility transistors (HEMTs) [11]. 2DEG means that the electron gas can move in two dimensions freely but is confined in the third. The AlGa_N/Ga_N interface is used because the materials have different bandgaps and polarizations, and free electrons are transferred from the AlGa_N to the Ga_N layers [11]. HEMTs are used for switching and are capable of high-power performance in applications such as radars, satellites, and base-station transmitters [11, 76].

Due to the high powers and high heats that these materials operate at, the thermal properties are an important consideration for device performance. These materials have shown irreversible degradation at temperatures above 600 °C [78], and there was a decrease in electron mobility and degradation in RF performance at higher temperatures [79, 80]. Thermal resistance measurements of AlGa_N/Ga_N HEMTs have been studied in the past [81, 82]. However, the Ga_N that we used was seed-grown, creating a grain size gradient that increasing in size from the nucleation point outward. Grain-graded materials could lead to thermal rectification, direction dependent thermal transport, due to differences in phonon scattering in different directions [83]. This work seeks to explore the thermal properties of

grain-graded GaN in an AlGa_N/Ga_N material system.

6.1 Material Stack

The sample studied was a material stack that consisted of an 80 nm Au/5 nm Ti transducer, 120 nm SiN, 16 nm AlGa_N, 1 nm AlN (2DEG), 1.6 μ m Ga_N, and a silicon substrate. For our thermal analysis, the AlN can be treated as a boundary due to its small relative thickness. To determine the directional dependent thermal properties, the substrate was etched on the bottom and coated with a transducer to allow for measurement on both sides. A diagram of the material stack is shown in Figure 6.1.

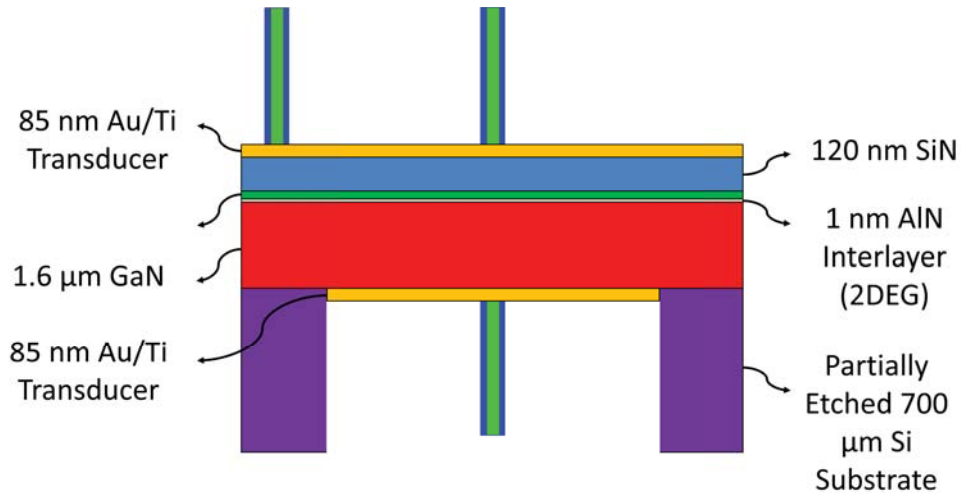


Figure 6.1: Diagram of the GaN material stack. These materials were etched on the bottom and coated with the transducer on both sides. This allows the measurement from the top and bottom.

The diagram also shows the locations we studied on the same material: on the top over the etch, on the top over the substrate, and on the bottom on the etch.

6.2 Results and Discussion

To fit the data, we used published literature and commercial values of the thermal conductivity for AlGa_N and SiN as well as volumetric heat capacity for AlGa_N, Ga_N, and SiN. The thermal properties of Si were taken from the reference scans discussed in Chapter 2.3.

The thermal properties were assumed to be literature values in order to limit the number of fitted parameters. These assumed values are shown in Table 6.1. The volumetric heat capacity was found by multiplying specific heat with density.

Table 6.1: Assumed and measured properties used to fit the GaN data.

Material	κ [$W\ m^{-1}K^{-1}$]	C_v [$MJ\ m^{-3}K^{-1}$]
Au	200	2.5
SiN	30 [84]	2.4 [85]
AlGaN	13 [86]	2.9 [13, 87]
GaN	-	3.0 [87]
Si	138	1.6

The thermal properties of GaN was determined by running a five parameter fit for κ_{GaN} and the thermal boundary conductances between each layer (Transducer/SiN, SiN/AlGaN, AlGaN/GaN, and either GaN/Transducer or GaN/Si). These are numbered G_1 to G_4 , respectively. The FDTR scans and curve fits are shown below in Figure 6.2. The sensitivity plots are shown in Figure 6.3. The regressed parameters are listed in Table 6.2.

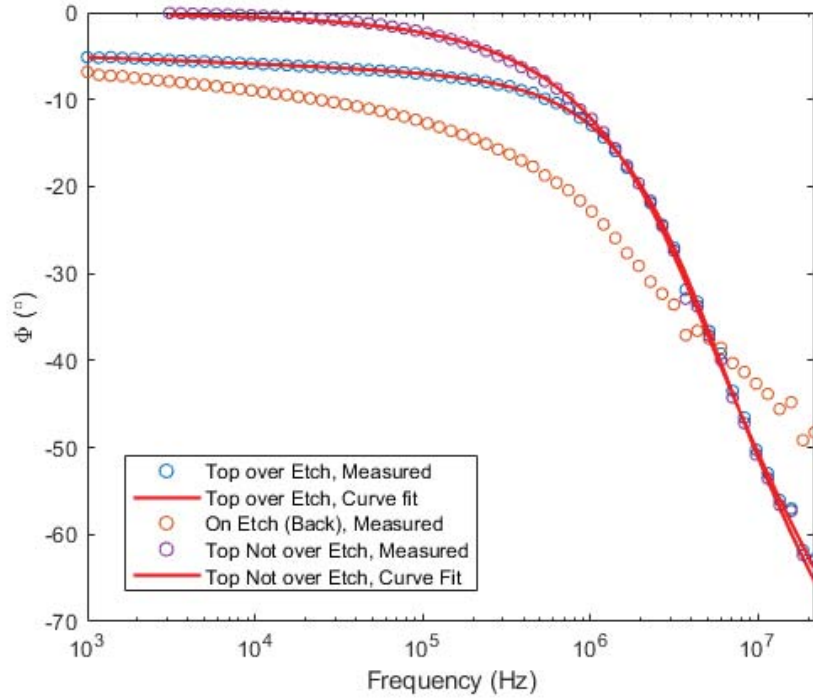


Figure 6.2: FDTR Scans and Curve Fits for GaN material stack.

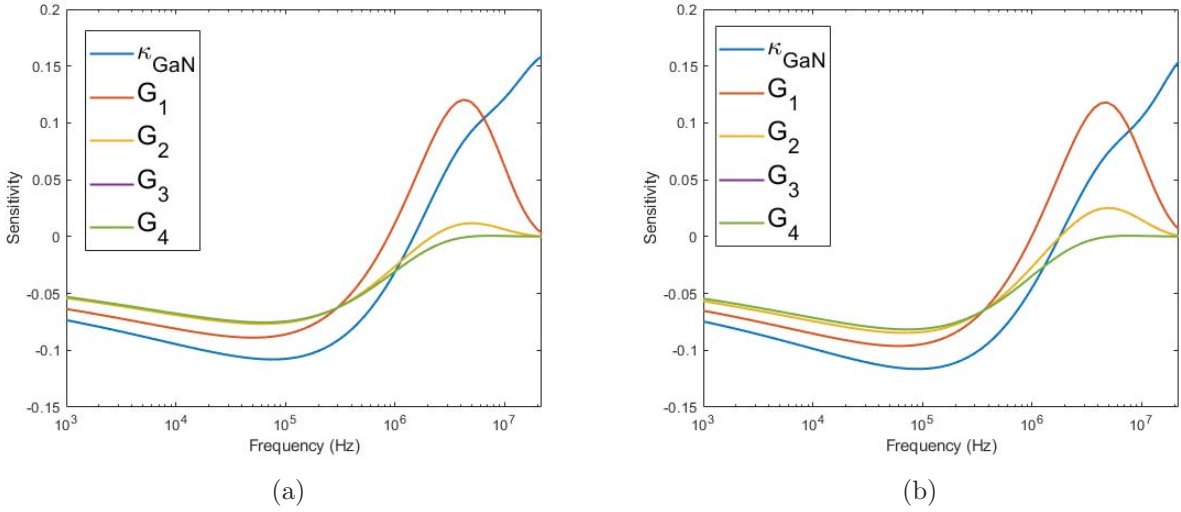


Figure 6.3: (a) Sensitivity plot of GaN stack measured from the top over the etch. (b) Sensitivity plot of GaN stack measured from the top over the substrate.

Table 6.2: Regressed parameters for GaN material stack

Thermal Property	Top over Etch	Top over Substrate
κ_{GaN} [$\text{W m}^{-1}\text{K}^{-1}$]	167.2 ± 16.3	154.6 ± 9.3
G_1 [$\text{MW m}^{-2}\text{K}^{-1}$]	11.4 ± 0.3	13.4 ± 3.7
G_2 [$\text{MW m}^{-2}\text{K}^{-1}$]	19.6 ± 0.8	22.5 ± 1.9
G_3 [$\text{MW m}^{-2}\text{K}^{-1}$]	196 ± 11.8	104 ± 5.1
G_4 [$\text{MW m}^{-2}\text{K}^{-1}$]	1490 ± 367	3270 ± 2070

As shown from the results, the two thermal conductivities measured from the top were similar as expected. One thing to note is that the sensitivities of all of the parameters with the exception of thermal conductivity had similar peaks, and the sensitivity for thermal boundary conductance decreased further into the stack. This suggests that the thermal boundary conductance values may not have been accurate. Because the thermal conductivity had a different peak, it was able to be determined from the study.

However, we were not able to fit the data from scanning the bottom with our current FDTR model. It may suggest a difference in thermal properties depending on the direction. Another reason was that our current thermal model did not account for differences in grain size throughout the GaN layer; it treated the GaN as having uniform material properties.

Instead of solving the heat equation using the matrix method discussed in Chapter 2.2,

we will utilize a COMSOL model that incorporates the Callaway model. Using this model, we can include a depth dependent grain size and its effect on the thermal properties due to grain boundary scattering.

6.3 Conclusions

We measured the thermal conductivity of grain graded GaN in an 80 nm Au/5 nm Ti/16nm AlGaN/1 nm AlN/1.6 μm GaN/700 μm Si material stack. Part of the Si substrate was etched to allow probing on both sides. The measured thermal conductivity was 167.2 ± 16.3 W m⁻¹K⁻¹ when measured from the top over the etch and 154.6 ± 9.3 W m⁻¹K⁻¹ when measured from the top over the substrate. We were unable to fit the data when measured from the bottom. We will incorporate a COMSOL/Callaway model to incorporate the effects of grain boundary scattering to fit the data in the near future.

Conclusions

Four nanostructured materials used in a wide variety of electronic applications were studied using frequency domain thermoreflectance to better understand the nanoscale heat transfer. The FDTR system was built over the course of this project, and it was validated using glass, sapphire, and silicon, reference materials with known thermal properties. Temperature dependent measurements were validated using sapphire. For all of these reference samples, the thermal conductivity agreed well with literature values.

The first electronic material studied was nickel titanium, where we investigated the effects of grain size on the thermal conductivity at both ends of the martensitic phase transformation. Using FDTR, thermal conductivity as a function of temperature was measured for NiTi samples with different grain sizes and found that the thermal conductivity increases with grain size. The results also suggest that grain boundary scattering was likely the dominant transport mechanism for these materials for the nano-grained sample.

The second material studied were thin films of germanium telluride. We found that the thermal conductivity decreased with decreasing film thickness, suggesting that the mean free path approached that of the film thickness. By fitting a kinetic theory of gases model, we found that the intrinsic mean free paths were similar for both the amorphous and crystalline samples: 63 nm for the crystalline and 45 nm for the amorphous.

The third study was on $\text{Bi}_2\text{Te}_3/\text{Bi}_2(\text{TeSe})_3$ superlattices. Three samples were studied, and we found a high amount of anisotropy, a significant increase in Lorenz number, and in-plane thermal conductivity values much larger than bulk. We will need to conduct more studies to understand, but we suspect that we are activating the topological insulator effect. The last study was on an AlGaIn/GaN HEMTs structure where the GaN was seed-grown, resulting in a grain gradient. When measured from the top, the thermal conductivity were similar. However, we were unable to fit the data from the bottom. This may have been caused by differences in thermal transport due to the grain-gradient. We will incorporate a

grain-dependent Callaway model in COMSOL to study this material.

By diving into the nano-scale realm of heat transfer, we have observed interesting phenomena that could be incorporated into new technologies and applications. Studies in this field are essential for the improvement of electronics as the characteristic sizes continue to decrease. By altering the properties in the nanoscale, we can drastically affect the macroscale.

References

- [1] P. L. Komarov, M. G. Burzo, and P. E. Raad, "A thermoreflectance thermography system for measuring the transient surface temperature field of activated electronic devices," in *Twenty-Second Annual IEEE Semiconductor Thermal Measurement And Management Symposium*, March 2006, pp. 199–203.
- [2] D. G. Cahill, "Thermal conductivity data: Sapphire." [Online]. Available: <https://cahill.matse.illinois.edu/software-and-data/>
- [3] G. P. Chen, *Nanoscale Energy Transport and Conversion: A Parallel Treatment of Electrons, Molecules, Phonons, and Photons*. Oxford University Press, 2005.
- [4] D. J. Sharar, J. Radice, R. Warzoha, B. Hanrahan, and B. Chang, "First demonstration of a bending-mode elastocaloric cooling loop," in *2018 17th IEEE Intersociety Conference on Thermal and Thermomechanical Phenomena in Electronic Systems (ITherm)*, May 2018, pp. 218–226.
- [5] D. J. Sharar, B. F. Donovan, R. J. Warzoha, A. A. Wilson, A. C. Leff, and B. M. Hanrahan, "Solid-state thermal energy storage using reversible martensitic transformations," *Applied Physics Letters*, vol. 114, no. 14, p. 143902, 2019. [Online]. Available: <https://doi.org/10.1063/1.5087135>
- [6] A. Chen, S. Haddad, Y.-C. Wu, T.-N. Fang, Z. Lan, S. Avanzino, S. Pangrle, M. Buynoski, M. Rathor, W. Cai, N. Tripsas, C. Bill, M. V. Buskirk, and M. Taguchi, "Non-volatile resistive switching for advanced memory applications," in *IEEE International Electron Devices Meeting, 2005. IEDM Technical Digest.*, 2005, pp. 746–749.
- [7] M. Chen, K. A. Rubin, and R. W. Barton, "Compound materials for reversible, phasechange optical data storage," *Applied Physics Letters*, vol. 49, no. 9, pp. 502–504, 1986. [Online]. Available: <https://doi.org/10.1063/1.97617>
- [8] M. Wuttig, H. Bhaskaran, and T. Taubner, "Phase change materials for non-volatile photonic applications," *Nature Photonics*, vol. 11, no. 8, p. 465476, 2017.
- [9] M. H. Elsheikh, D. A. Shnawah, M. F. M. Sabri, S. B. M. Said, M. H. Hassan, M. B. A. Bashir, and M. Mohamad, "A review on thermoelectric renewable energy: Principle parameters that affect their performance," *Renewable and Sustainable Energy Reviews*, vol. 30, pp. 337 – 355, 2014. [Online]. Available: <http://www.sciencedirect.com/science/article/pii/S1364032113007260>
- [10] M. Z. Hasan and C. L. Kane, "Colloquium: Topological insulators," *Rev. Mod. Phys.*, vol. 82, pp. 3045–3067, Nov 2010. [Online]. Available: <https://link.aps.org/doi/10.1103/RevModPhys.82.3045>
- [11] M. H. Rashid. Elsevier, 2018. [Online]. Available: <https://app.knovel.com/hotlink/toc/id:kpPEHE000C/power-electronics-handbook/power-electronics-handbook>

-
- [12] C. Kittel, P. McEuen, and P. McEuen, *Introduction to solid state physics*. Wiley New York, 1976, vol. 8.
- [13] F. P. Incropera, D. P. DeWitt, T. L. Bergman, and A. S. Lavine, *Introduction to Heat Transfer*. John Wiley & Sons, 2006.
- [14] M. Asheghi, K. Kurabayashi, R. Kasnavi, and K. E. Goodson, “Thermal conduction in doped single-crystal silicon films,” *Journal of Applied Physics*, vol. 91, no. 8, pp. 5079–5088, 2002. [Online]. Available: <https://doi.org/10.1063/1.1458057>
- [15] J. Callaway, “Model for lattice thermal conductivity at low temperatures,” *Phys. Rev.*, vol. 113, pp. 1046–1051, Feb 1959. [Online]. Available: <https://link.aps.org/doi/10.1103/PhysRev.113.1046>
- [16] B. Donovan, “Understanding phonon interactions with defects in functional oxide materials,” Ph.D. dissertation, Online Archive of University of Virginia Scholarship, Jul 2016. [Online]. Available: <https://doi.org/10.18130/V30W21>
- [17] M. Asheghi, Y. K. Leung, S. S. Wong, and K. E. Goodson, “Phonon-boundary scattering in thin silicon layers,” *Applied Physics Letters*, vol. 71, no. 13, pp. 1798–1800, 1997. [Online]. Available: <https://doi.org/10.1063/1.119402>
- [18] R. Berman, “The thermal conductivity of some polycrystalline solids at low temperatures,” *Proceedings of the Physical Society. Section A*, vol. 65, no. 12, pp. 1029–1040, dec 1952. [Online]. Available: <https://doi.org/10.1088%2F0370-1298%2F65%2F12%2F311>
- [19] A. J. Schmidt, R. Cheaito, and M. Chiesa, “A frequency-domain thermoreflectance method for the characterization of thermal properties,” *Review of Scientific Instruments*, vol. 80, no. 9, p. 094901, 2009. [Online]. Available: <https://doi.org/10.1063/1.3212673>
- [20] J. Yang, “Thermal property measurement with frequency domain thermoreflectance,” Ph.D. dissertation, Boston University College of Engineering, 2016. [Online]. Available: <https://open.bu.edu/handle/2144/17057>
- [21] P. Jiang, X. Qian, and R. Yang, “Tutorial: Time-domain thermoreflectance (tdtr) for thermal property characterization of bulk and thin film materials,” *Journal of Applied Physics*, vol. 124, no. 16, p. 161103, 2018. [Online]. Available: <https://doi.org/10.1063/1.5046944>
- [22] D. G. Cahill, “Thermal conductivity measurement from 30 to 750 k: the 3 method,” *Review of Scientific Instruments*, vol. 61, no. 2, pp. 802–808, 1990. [Online]. Available: <https://doi.org/10.1063/1.1141498>
- [23] R. B. Wilson and D. G. Cahill, “Limits to fourier theory in high thermal conductivity single crystals,” *Applied Physics Letters*, vol. 107, no. 20, p. 203112, 2015. [Online]. Available: <https://doi.org/10.1063/1.4935987>

-
- [24] L. Lecce and A. Concilio, *Shape Memory Alloy Engineering: for Aerospace, Structural and Biomedical Applications*, 1st ed. Butterworth-Heinemann, 2015.
 - [25] N. Simha, P. R. Sreekanth, and S. V. Siva, “Shape-memory alloys,” in *Reference Module in Materials Science and Materials Engineering*. Elsevier, 2017. [Online]. Available: <http://www.sciencedirect.com/science/article/pii/B9780128035818008742>
 - [26] N. Morgan, “Medical shape memory alloy applications the market and its products,” *Materials Science and Engineering: A*, vol. 378, no. 1, pp. 16 – 23, 2004, european Symposium on Martensitic Transformation and Shape-Memory. [Online]. Available: <http://www.sciencedirect.com/science/article/pii/S0921509303015132>
 - [27] F. J. Gil and J. A. Planell, “Shape memory alloys for medical applications,” *Proceedings of the Institution of Mechanical Engineers, Part H: Journal of Engineering in Medicine*, vol. 212, no. 6, pp. 473–488, 1998, pMID: 9852742. [Online]. Available: <https://doi.org/10.1243/0954411981534231>
 - [28] D. J. Hartl and D. C. Lagoudas, “Aerospace applications of shape memory alloys,” *Proceedings of the Institution of Mechanical Engineers*, vol. 221, pp. 535–552, 08 2007, copyright - Copyright Professional Engineering Publishing Ltd Aug 2007; Document feature - Tables; ; Graphs; Diagrams; Photographs; Last updated - 2016-04-23. [Online]. Available: <https://search.proquest.com/docview/213182302?accountid=14748>
 - [29] G. Song, N. Ma, and H.-N. Li, “Applications of shape memory alloys in civil structures,” *Engineering Structures*, vol. 28, no. 9, pp. 1266 – 1274, 2006. [Online]. Available: <http://www.sciencedirect.com/science/article/pii/S0141029606000344>
 - [30] W. Goetzler, R. Zogg, J. Young, and C. Johnson, “Energy savings potential and rdd opportunities for non-vapor-copression hvac technologies,” U.S. Department of Energy, Burlington, MA, Tech. Rep., March 2014.
 - [31] S. Qian, Y. Geng, Y. Wang, J. Ling, Y. Hwang, R. Radermacher, I. Takeuchi, and J. Cui, “A review of elastocaloric cooling: Materials, cycles and system integrations,” *International Journal of Refrigeration*, vol. 64, pp. 1 – 19, 2016. [Online]. Available: <http://www.sciencedirect.com/science/article/pii/S0140700715003783>
 - [32] J. Cui, Y. Wu, J. Muehlbauer, Y. Hwang, R. Radermacher, S. Fackler, M. Wuttig, and I. Takeuchi, “Demonstration of high efficiency elastocaloric cooling with large t using niti wires,” *Applied Physics Letters*, vol. 101, no. 7, p. 073904, 2012. [Online]. Available: <https://doi.org/10.1063/1.4746257>
 - [33] D. J. Sharar, J. Radice, R. Warzoha, B. Hanrahan, and B. Chang, “First demonstration of a bending-mode elastocaloric cooling loop,” in *2018 17th IEEE Intersociety Conference on Thermal and Thermomechanical Phenomena in Electronic Systems (ITherm)*, May 2018, pp. 218–226.
 - [34] H. Ossmer, C. Chluba, S. Kauffmann-Weiss, E. Quandt, and M. Kohl, “Tini-based films for elastocaloric microcooling fatigue life and device performance,” *APL Materials*, vol. 4, no. 6, p. 064102, 2016. [Online]. Available: <https://doi.org/10.1063/1.4948271>

-
- [35] K. Otsuka and X. Ren, "Physical metallurgy of tni-based shape memory alloys," *Progress in Materials Science*, vol. 50, no. 5, pp. 511 – 678, 2005. [Online]. Available: <http://www.sciencedirect.com/science/article/pii/S0079642504000647>
- [36] Y. Terada, K. Ohkubo, T. Mohri, and T. Suzuki, "Thermal conductivity of intermetallic compounds with metallic bonding," *MATERIALS TRANSACTIONS*, vol. 43, no. 12, pp. 3167–3176, 2002.
- [37] M. Rohde and A. Schussler, "On the response-time behaviour of laser micromachined niti shape memory actuators," *Sensors and Actuators A: Physical*, vol. 61, no. 1, pp. 463 – 468, 1997, proceedings of EUROSENSORS X. [Online]. Available: <http://www.sciencedirect.com/science/article/pii/S0924424797803068>
- [38] M. G. Faulkner, J. J. Amalraj, and A. Bhattacharyya, "Experimental determination of thermal and electrical properties of ni-ti shape memory wires," *Smart Materials and Structures*, vol. 9, no. 5, p. 632, 2000. [Online]. Available: <http://stacks.iop.org/0964-1726/9/i=5/a=307>
- [39] A. Jain and K. E. Goodson, "Measurement of the thermal conductivity and heat capacity of freestanding shape memory thin films using the 3ω method," *Journal of Heat Transfer*, vol. 130, no. 10, p. 102402, 2008.
- [40] C. Zanotti, P. Giuliani, and A. Chrysanthou, "Martensiticaustenitic phase transformation of niti smas: Thermal properties," *Intermetallics*, vol. 24, pp. 106 – 114, 2012. [Online]. Available: <http://www.sciencedirect.com/science/article/pii/S0966979512000489>
- [41] A. Ahadi and Q. Sun, "Stress hysteresis and temperature dependence of phase transition stress in nanostructured nitieffects of grain size," *Applied Physics Letters*, vol. 103, no. 2, p. 021902, 2013. [Online]. Available: <https://doi.org/10.1063/1.4812643>
- [42] S. Khademzadeh, N. Parvin, and P. F. Bariani, "Production of niti alloy by direct metal deposition of mechanically alloyed powder mixtures," *International Journal of Precision Engineering and Manufacturing*, vol. 16, no. 11, pp. 2333–2338, Oct 2015. [Online]. Available: <https://doi.org/10.1007/s12541-015-0300-1>
- [43] M. Wuttig and N. Yamada, "Phase-change materials for rewriteable data storage," *Nature Materials*, vol. 6, pp. 824 EP –, Nov 2007, review Article. [Online]. Available: <https://doi.org/10.1038/nmat2009>
- [44] H. F. Hamann, M. O'Boyle, Y. C. Martin, M. Rooks, and H. K. Wickramasinghe, "Ultra-high-density phase-change storage and memory," *Nature Materials*, vol. 5, no. 5, pp. 383–387, 2006. [Online]. Available: <https://doi.org/10.1038/nmat1627>
- [45] G. Bruns, P. Merkelbach, C. Schlockermann, M. Salinga, M. Wuttig, T. D. Happ, J. B. Philipp, and M. Kund, "Nanosecond switching in gete phase change memory cells," *Applied Physics Letters*, vol. 95, no. 4, p. 043108, 2009. [Online]. Available: <https://doi.org/10.1063/1.3191670>

-
- [46] R. Lan, R. Endo, M. Kuwahara, Y. Kobayashi, and M. Susa, “Electrical and heat conduction mechanisms of gete alloy for phase change memory application,” *Journal of Applied Physics*, vol. 112, no. 5, p. 053712, 2012. [Online]. Available: <https://doi.org/10.1063/1.4751018>
 - [47] N. El-Hinnawy, P. Borodulin, B. Wagner, M. R. King, J. S. Mason, E. B. Jones, S. McLaughlin, V. Veliadis, M. Snook, M. E. Sherwin, R. S. Howell, R. M. Young, and M. J. Lee, “A four-terminal, inline, chalcogenide phase-change rf switch using an independent resistive heater for thermal actuation,” *IEEE Electron Device Letters*, vol. 34, no. 10, pp. 1313–1315, 2013.
 - [48] J. G. Champlain, L. B. Ruppalt, A. C. Guyette, N. El-Hinnawy, P. Borodulin, E. Jones, R. M. Young, and D. Nichols, “Examination of the temperature dependent electronic behavior of gete for switching applications,” *Journal of Applied Physics*, vol. 119, no. 24, p. 244501, 2016. [Online]. Available: <https://doi.org/10.1063/1.4954313>
 - [49] E. M. Levin, M. F. Besser, and R. Hanus, “Electronic and thermal transport in gete: A versatile base for thermoelectric materials,” *Journal of Applied Physics*, vol. 114, no. 8, p. 083713, 2013. [Online]. Available: <https://doi.org/10.1063/1.4819222>
 - [50] D. Campi, L. Paulatto, G. Fugallo, F. Mauri, and M. Bernasconi, “First-principles calculation of lattice thermal conductivity in crystalline phase change materials: Gete, sb_2te_3 , and $\text{ge}_2\text{sb}_2\text{te}_5$,” *Phys. Rev. B*, vol. 95, p. 024311, Jan 2017. [Online]. Available: <https://link.aps.org/doi/10.1103/PhysRevB.95.024311>
 - [51] F. Serrano-Snchez, M. Funes, N. M. Nemes, O. J. Dura, J. L. Martnez, J. Prado-Gonjal, M. T. Fernandez-Daz, and J. A. Alonso, “Low lattice thermal conductivity in arc-melted gete with ge-deficient crystal structure,” *Applied Physics Letters*, vol. 113, no. 8, p. 083902, 2018. [Online]. Available: <https://doi.org/10.1063/1.5043359>
 - [52] A. Majumdar, “Microscale heat conduction in dielectric thin films,” *Journal of Heat Transfer*, vol. 115, no. 1, pp. 7–16, Feb 1993. [Online]. Available: <http://dx.doi.org/10.1115/1.2910673>
 - [53] G. Chen and A. Shakouri, “Heat transfer in nanostructures for solid-state energy conversion,” *Journal of Heat Transfer*, vol. 124, no. 2, pp. 242–252, Nov 2001. [Online]. Available: <http://dx.doi.org/10.1115/1.1448331>
 - [54] D. G. Cahill, P. V. Braun, G. Chen, D. R. Clarke, S. Fan, K. E. Goodson, P. Keblinski, W. P. King, G. D. Mahan, A. Majumdar, H. J. Maris, S. R. Phillpot, E. Pop, and L. Shi, “Nanoscale thermal transport. ii. 20032012,” *Applied Physics Reviews*, vol. 1, no. 1, p. 011305, 2014. [Online]. Available: <https://doi.org/10.1063/1.4832615>
 - [55] M. Asheghi, Y. K. Leung, S. S. Wong, and K. E. Goodson, “Phonon-boundary scattering in thin silicon layers,” *Applied Physics Letters*, vol. 71, no. 13, pp. 1798–1800, 1997. [Online]. Available: <https://doi.org/10.1063/1.119402>

-
- [56] P. Nath and K. L. Chopra, “Thermal conductivity of amorphous and crystalline ge and gete films,” *Phys. Rev. B*, vol. 10, pp. 3412–3418, Oct 1974. [Online]. Available: <https://link.aps.org/doi/10.1103/PhysRevB.10.3412>
 - [57] J. L. Bosse, M. Timofeeva, P. D. Tovee, B. J. Robinson, B. D. Huey, and O. V. Kolosov, “Nanothermal characterization of amorphous and crystalline phases in chalcogenide thin films with scanning thermal microscopy,” *Journal of Applied Physics*, vol. 116, no. 13, p. 134904, 2014. [Online]. Available: <https://doi.org/10.1063/1.4895493>
 - [58] R. Fallica, E. Varesi, L. Fumagalli, S. Spadoni, M. Longo, and C. Wiemer, “Effect of nitrogen doping on the thermal conductivity of gete thin films,” *physica status solidi (RRL) Rapid Research Letters*, vol. 7, no. 12, pp. 1107–1111, 2013. [Online]. Available: <https://onlinelibrary.wiley.com/doi/abs/10.1002/pssr.201308026>
 - [59] J. E. Moore, “The birth of topological insulators,” *Nature*, vol. 464, pp. 194 EP –, Mar 2010. [Online]. Available: <https://doi.org/10.1038/nature08916>
 - [60] X.-L. Qi and S.-C. Zhang, “Topological insulators and superconductors,” *Rev. Mod. Phys.*, vol. 83, pp. 1057–1110, Oct 2011. [Online]. Available: <https://link.aps.org/doi/10.1103/RevModPhys.83.1057>
 - [61] L. Fu, C. L. Kane, and E. J. Mele, “Topological insulators in three dimensions,” *Phys. Rev. Lett.*, vol. 98, p. 106803, Mar 2007. [Online]. Available: <https://link.aps.org/doi/10.1103/PhysRevLett.98.106803>
 - [62] Y. L. Chen, J. G. Analytis, J.-H. Chu, Z. K. Liu, S.-K. Mo, X. L. Qi, H. J. Zhang, D. H. Lu, X. Dai, Z. Fang, S. C. Zhang, I. R. Fisher, Z. Hussain, and Z.-X. Shen, “Experimental realization of a three-dimensional topological insulator, Bi_2Te_3 ,” *Science*, vol. 325, no. 5937, pp. 178–181, 2009. [Online]. Available: <http://science.sciencemag.org/content/325/5937/178>
 - [63] H. Zhang, C.-X. Liu, X.-L. Qi, X. Dai, Z. Fang, and S.-C. Zhang, “Topological insulators in Bi_2Se_3 , Bi_2Te_3 and Sb_2Te_3 with a single dirac cone on the surface,” *Nature Physics*, vol. 5, pp. 438 EP –, May 2009, article. [Online]. Available: <https://doi.org/10.1038/nphys1270>
 - [64] L. Mehler, F. Casper, B. Yan, S. Chadov, and C. Felser, “Topological insulators and thermoelectric materials,” *physica status solidi (RRL) Rapid Research Letters*, vol. 7, no. 12, pp. 91–100, 2013. [Online]. Available: <https://onlinelibrary.wiley.com/doi/abs/10.1002/pssr.201206411>
 - [65] N. Xu, Y. Xu, and J. Zhu, “Topological insulators for thermoelectrics,” *npj Quantum Materials*, vol. 2, no. 1, p. 51, 2017. [Online]. Available: <https://doi.org/10.1038/s41535-017-0054-3>
 - [66] B. Poudel, Q. Hao, Y. Ma, Y. Lan, A. Minnich, B. Yu, X. Yan, D. Wang, A. Muto, D. Vashaee, X. Chen, J. Liu, M. S. Dresselhaus, G. Chen, and Z. Ren, “High-thermoelectric performance of nanostructured bismuth antimony telluride

- bulk alloys,” *Science*, vol. 320, no. 5876, pp. 634–638, 2008. [Online]. Available: <http://science.sciencemag.org/content/320/5876/634>
- [67] H. Mamur, M. Bhuiyan, F. Korkmaz, and M. Nil, “A review on bismuth telluride (bi₂te₃) nanostructure for thermoelectric applications,” *Renewable and Sustainable Energy Reviews*, vol. 82, pp. 4159 – 4169, 2018. [Online]. Available: <http://www.sciencedirect.com/science/article/pii/S1364032117314855>
- [68] R. Venkatasubramanian, E. Siivola, T. Colpitts, and B. O’Quinn, “Thin-film thermoelectric devices with high room-temperature figures of merit,” *Nature*, vol. 413, no. 6856, pp. 597–602, 2001. [Online]. Available: <https://doi.org/10.1038/35098012>
- [69] B. Yang, W. L. Liu, J. L. Liu, K. L. Wang, and G. Chen, “Measurements of anisotropic thermoelectric properties in superlattices,” *Applied Physics Letters*, vol. 81, no. 19, pp. 3588–3590, 2002. [Online]. Available: <https://doi.org/10.1063/1.1515876>
- [70] R. T. Delves, A. E. Bowley, D. W. Hazelden, and H. J. Goldsmid, “Anisotropy of the electrical conductivity in bismuth telluride,” *Proceedings of the Physical Society*, vol. 78, no. 5, pp. 838–844, nov 1961. [Online]. Available: <https://doi.org/10.1088%2F0370-1328%2F78%2F5%2F329>
- [71] M. N. Touzelbaev, P. Zhou, R. Venkatasubramanian, and K. E. Goodson, “Thermal characterization of bi₂te₃/sb₂te₃ superlattices,” *Journal of Applied Physics*, vol. 90, no. 2, pp. 763–767, 2001. [Online]. Available: <https://doi.org/10.1063/1.1374458>
- [72] B.-L. Huang and M. Kaviany, “Ab initio and molecular dynamics predictions for electron and phonon transport in bismuth telluride,” *Phys. Rev. B*, vol. 77, p. 125209, Mar 2008. [Online]. Available: <https://link.aps.org/doi/10.1103/PhysRevB.77.125209>
- [73] Z. Luo, J. Tian, S. Huang, M. Srinivasan, J. Maassen, Y. P. Chen, and X. Xu, “Large enhancement of thermal conductivity and lorenz number in topological insulator thin films,” *ACS Nano*, vol. 12, no. 2, pp. 1120–1127, 2018, pMID: 29361229. [Online]. Available: <https://doi.org/10.1021/acsnano.7b06430>
- [74] H. J. Goldsmid, “The thermal conductivity of bismuth telluride,” *Proceedings of the Physical Society. Section B*, vol. 69, no. 2, pp. 203–209, feb 1956. [Online]. Available: <https://doi.org/10.1088%2F0370-1301%2F69%2F2%2F310>
- [75] M. T. Pettes, J. Maassen, I. Jo, M. S. Lundstrom, and L. Shi, “Effects of surface band bending and scattering on thermoelectric transport in suspended bismuth telluride nanoplates,” *Nano Letters*, vol. 13, no. 11, pp. 5316–5322, 2013, pMID: 24164564. [Online]. Available: <https://doi.org/10.1021/nl402828s>
- [76] U. K. Mishra and P. P. and, “Algan/gan hemts-an overview of device operation and applications,” *Proceedings of the IEEE*, vol. 90, no. 6, pp. 1022–1031, June 2002.
- [77] Y. . Wu, A. Saxler, M. Moore, R. P. Smith, S. Sheppard, P. M. Chavarkar, T. Wisleder, U. K. Mishra, and P. Parikh, “30-w/mm gan hemts by field plate optimization,” *IEEE Electron Device Letters*, vol. 25, no. 3, pp. 117–119, March 2004.

-
- [78] I. Daumiller, C. Kirchner, M. Kamp, K. J. Ebeling, and E. Kohn, "Evaluation of the temperature stability of algan/gan heterostructure fets," *IEEE Electron Device Letters*, vol. 20, no. 9, pp. 448–450, Sep. 1999.
 - [79] M. W. Shin and R. J. Trew, "Gan mesfets for high-power and high-temperature microwave applications," *Electronics Letters*, vol. 31, no. 6, pp. 498–500, March 1995.
 - [80] S. Vitanov, V. Palankovski, S. Maroldt, and R. Quay, "High-temperature modeling of algan/gan hemts," *Solid-State Electronics*, vol. 54, no. 10, pp. 1105 – 1112, 2010, selected Papers from ISDRS 2009. [Online]. Available: <http://www.sciencedirect.com/science/article/pii/S0038110110002017>
 - [81] M. Kuball, S. Rajasingam, A. Sarua, M. J. Uren, T. Martin, B. T. Hughes, K. P. Hilton, and R. S. Balmer, "Measurement of temperature distribution in multifinger algan/gan heterostructure field-effect transistors using micro-raman spectroscopy," *Applied Physics Letters*, vol. 82, no. 1, pp. 124–126, 2003. [Online]. Available: <https://doi.org/10.1063/1.1534935>
 - [82] J. Kuzmik, S. Bychikhin, M. Neuburger, A. Dadgar, A. Krost, E. Kohn, and D. Pogany, "Transient thermal characterization of algan/gan hemts grown on silicon," *IEEE Transactions on Electron Devices*, vol. 52, no. 8, pp. 1698–1705, Aug 2005.
 - [83] Z. Cheng, B. M. Foley, T. Bougher, L. Yates, B. A. Cola, and S. Graham, "Thermal rectification in thin films driven by gradient grain microstructure," *Journal of Applied Physics*, vol. 123, no. 9, p. 095114, 2018. [Online]. Available: <https://doi.org/10.1063/1.5021681>
 - [84] "Silicon nitride, si3n4 ceramic properties." [Online]. Available: <https://www accuratus.com/silinit.html>
 - [85] R. Johnson, "Computational chemistry comparison and benchmark database, nist standard reference database 101," 2002. [Online]. Available: <http://cccbdb.nist.gov/>
 - [86] B. C. Daly, H. J. Maris, A. V. Nurmikko, M. Kuball, and J. Han, "Optical pump-and-probe measurement of the thermal conductivity of nitride thin films," *Journal of Applied Physics*, vol. 92, no. 7, pp. 3820–3824, 2002. [Online]. Available: <https://doi.org/10.1063/1.1505995>
 - [87] M. E. Levinshtein, S. L. Rumyantsev, and M. S. Shur, *Properties of Advanced Semiconductor Materials: GaN, AlN, InN, BN, SiC, SiGe*. J. Wiley and Sons, 2001.

Appendices

Appendix A FDTR Progression

Throughout the course of the project, the FDTR system went through many changes and faced even more challenges along the way. The FDTR system is by no means a turn-key system, and my expertise in the system took hundreds of hours to develop.

I began the project with a bare optical table without any lasers. This can be seen below in Figure A.1.

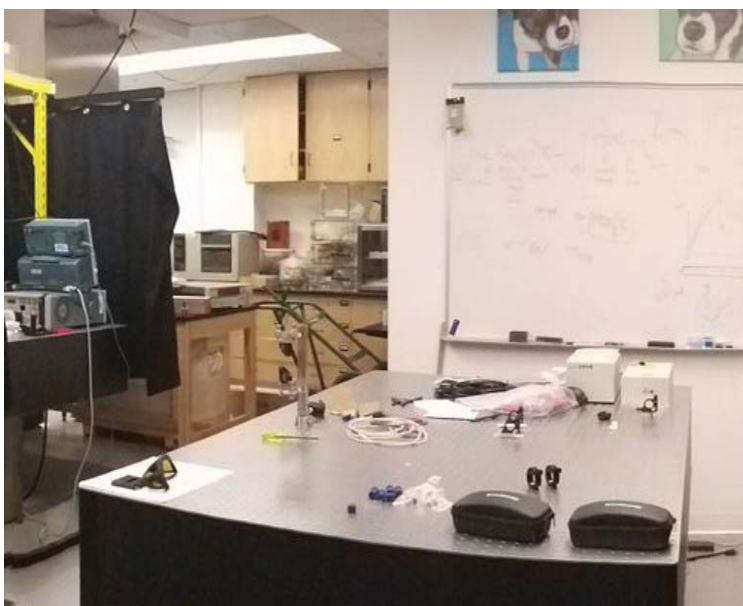


Figure A.1: Image of the bare optical table.

Over the course of a couple months, I began setting up the optical table, learning the basics of working with lasers. This included taking the necessary safety precautions and learning how to align lasers. The first configuration was a red (808 nm) pump, green (532 nm) probe system. The 532 nm laser came from the Millennia eV5, and part of this beam was the source of the Millennia 3900s laser cavity, which changed the wavelength to 808 nm. This configuration can be seen in Figure A.2.

With this system, my biggest problems were aligning through the electro-optic modulator

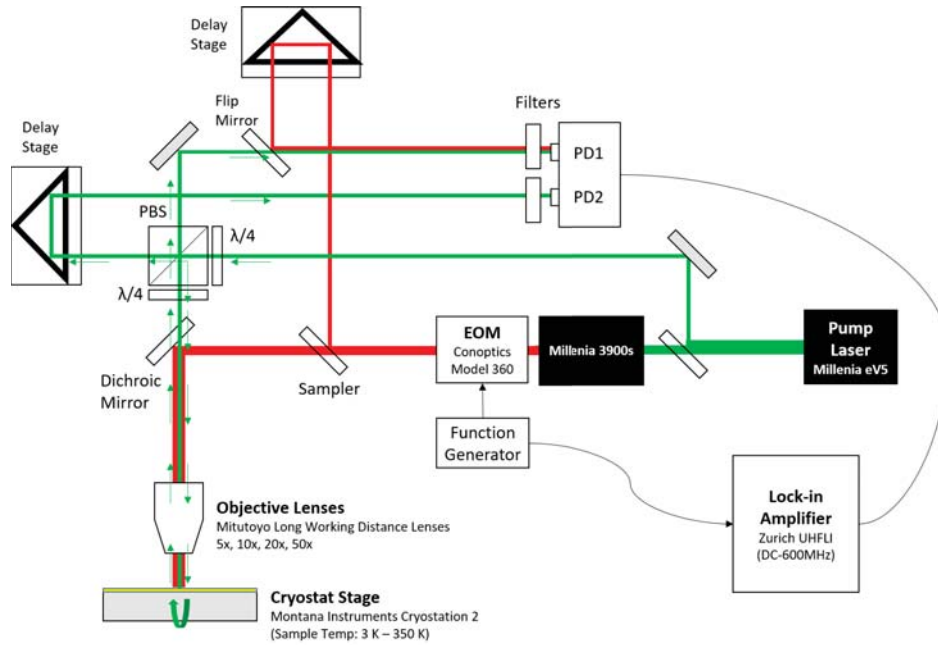


Figure A.2: Original FDTR setup with 532 nm probe, 808 nm pump.

(EOM) and figuring out how to properly modulate the signal using the lock-in amplifier. The EOM was much more sensitive to alignment compared to the other optics. Furthermore, the guides were unclear about the required voltage or termination needed to properly drive the EOM. The modulated signal would become distorted, become overwhelmed with noise, and even modulate at the wrong frequency. Over the period of weeks, we learned how to properly align through the EOM quickly and fix many of the issues by setting the proper termination, input signal, dc gain, and lock-in amplifier gain. We also needed to incorporate a linear polarizer, which we did not have at the time. We went from achieving this polarization with an old polarizing sheet, to using wave-plates and a polarizing beam cube, and to finally a normal input polarizer once the optics arrived.

Another recurring issue was with the Millenia 3900s cavity, which would repeatedly misalign and require hours to repair. This essentially halted all the progress during that day, as we had to focus on realignment.

Once we were able to take scans, they were not the cleanest due to noise. Figure A.3 is an example of an early scans of Si that was able to extract thermal properties with a level

of coherence.

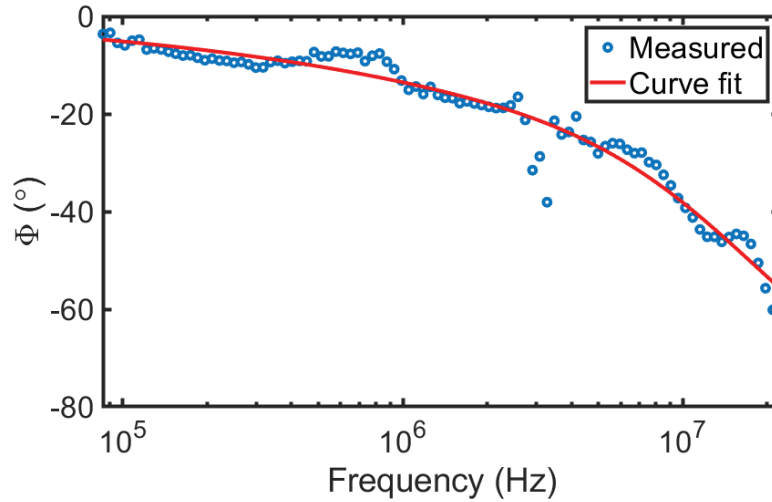


Figure A.3: Old FDTR scan of Si with a large amount of noise.

This resulted in a thermal conductivity of $188.8 \text{ W m}^{-1}\text{K}^{-1}$, thermal boundary conductance of $21.9 \text{ MW m}^{-2}\text{K}^{-1}$, and volumetric heat capacity of $0.68 \text{ MJ m}^{-3}\text{K}^{-1}$. The thermal conductivity was higher than the literature value of $133 \text{ W m}^{-1}\text{K}^{-1}$ [23].

An old scan of SiO_2 is shown in Figure A.4. The extracted thermal conductivity was $1.97 \text{ W m}^{-1}\text{K}^{-1}$, thermal boundary conductance was $280000 \text{ MW m}^{-2}\text{K}^{-1}$, and volumetric heat capacity was $3.45 \text{ MJ m}^{-3}\text{K}^{-1}$. The thermal conductivity value was high but relatively close to the literature value of 1.3 [22]. The thermal boundary conductance was unreasonably high.

As shown from both early scans, the thermal conductivity was able to be determined at the right order of magnitude, although both were high. This was due to the large amount of noise, which we determined to be caused by a variety of factors. We found that EOM problems, red backreflections, electronics near cables, alignment issues, and vibrations on the floor were significant noise sources. Most of these were fixed by better understanding how to operate the EOM, increasing the number of red filters, moving cables away from electronics, aligning more meticulously, floating the table, and later, using a signal amplifier. After implementing those fixes, we were able to obtain scans that look like the one

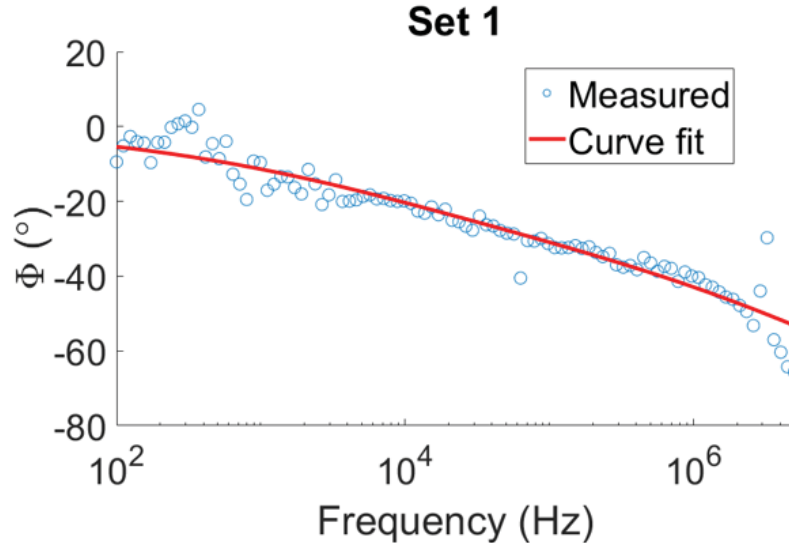


Figure A.4: Old FDTR scan of SiO_2 with a large amount of noise.

shown in Figure A.5.

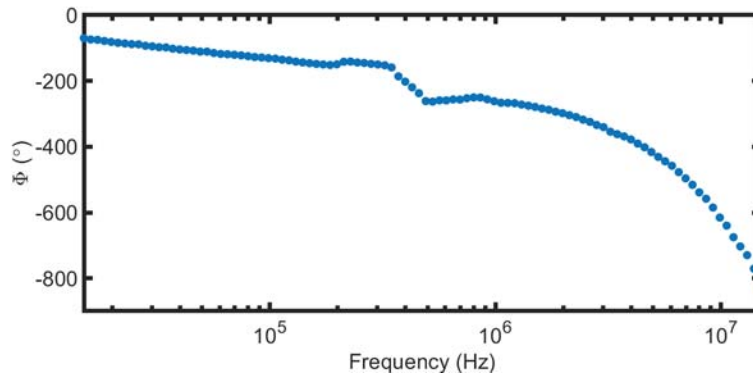


Figure A.5: Old FDTR scan with noise fixes.

Although less noisy overall, there was a noticeable "dip" around the 100-600 kHz range that we were unable to fix. This was a significant problem because that was a region where we were sensitive to a lot of thermal properties. This dip was ultimately attributed to phase noise from the the Millennia eV5 after analyzing the signal directly from the laser. Figure A.6 is a fast Fourier transform (FFT) analysis of the signal.

As shown from the FFT, there was a 60 kHz noise that propagated throughout. At the lower and higher frequencies, the lock-in amplifier is able to ignore it, but the hundreds of kHz region was where the lock-in was unable to resolve.

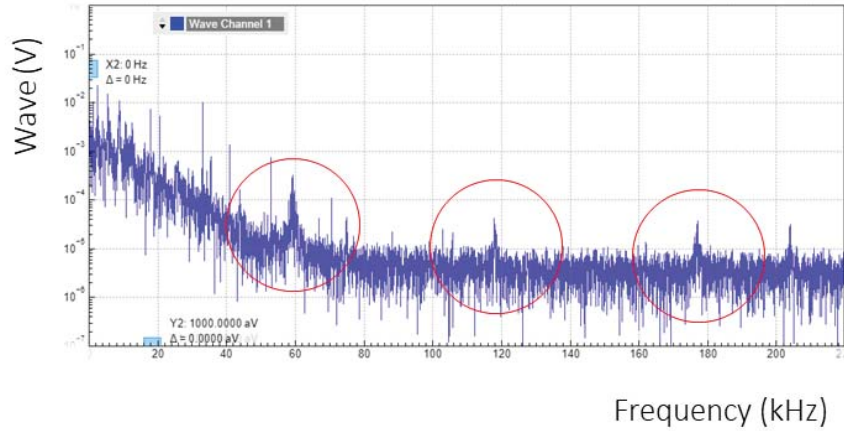


Figure A.6: FFT of signal from the Millenia eV5.

In order to fix this problem, Spectra-Physics had to rush a loaner Millenia eV10, which they installed special filters to reduced noise. Although the noise on this second laser was a lot less, it was still present. This is what lead us to order a blue (405 nm) laser, which we intended to use as our new pump. By doing so, we increase the amount of light absorbed by the transducer, increasing the thermal signal and therefore the signal-to-noise ratio. We purchased a 405 nm Obis LX diode laser for this purpose. However, we were unable to do this for another couple months because we had to wait for the order to come.

Nonetheless, we were able to obtain good results with the Millenia eV10. The FDTR scans of Si and SiO₂ are shown in Figure A.7. These scans were much better than before, and although there was some noticeable noise, there was significantly less.

These gave us thermal conductivity of $138 \text{ W m}^{-1}\text{K}^{-1}$, thermal boundary conductance of $3000000 \text{ MW m}^{-2}\text{K}^{-1}$, and volumetric heat capacity of $0.11 \text{ MJ m}^{-3}\text{K}^{-1}$ for Si. The thermal conductivity was close to the published value of $133 \text{ W m}^{-1}\text{K}^{-1}$ [23], although the thermal boundary conductance and volumetric heat capacity were unreasonable. The thermal conductivity of SiO₂ was spot on the literature value of 1.3 [22] with reasonable values for thermal boundary conductance and volumetric specific heat.

This was when we began to incorporate the cryostat, which turned out to be much more of a challenge than anticipated. An image of the cryostat is included in Figure A.8. For

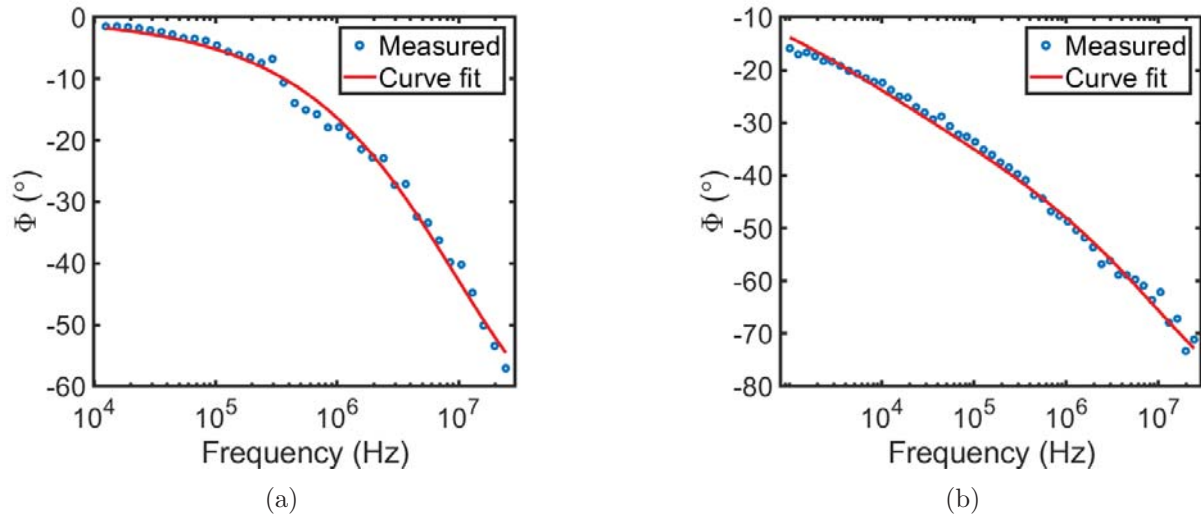


Figure A.7: (a) FDTR scan of Si from using the Millennia eV10. (b) FDTR scan of SiO_2 using the Millennia eV10.

one, it required significant changes to the optical table, as we had to move optics to fit the cryostat, and we had to path length match again. Furthermore, the cryostat required us to probe downwards instead of on a vertical mount. This made obtaining back reflection difficult, as the sample did not have a tilt stage. The cryostat was also time consuming, as we had to wait for it to heat and cool down before changing samples.

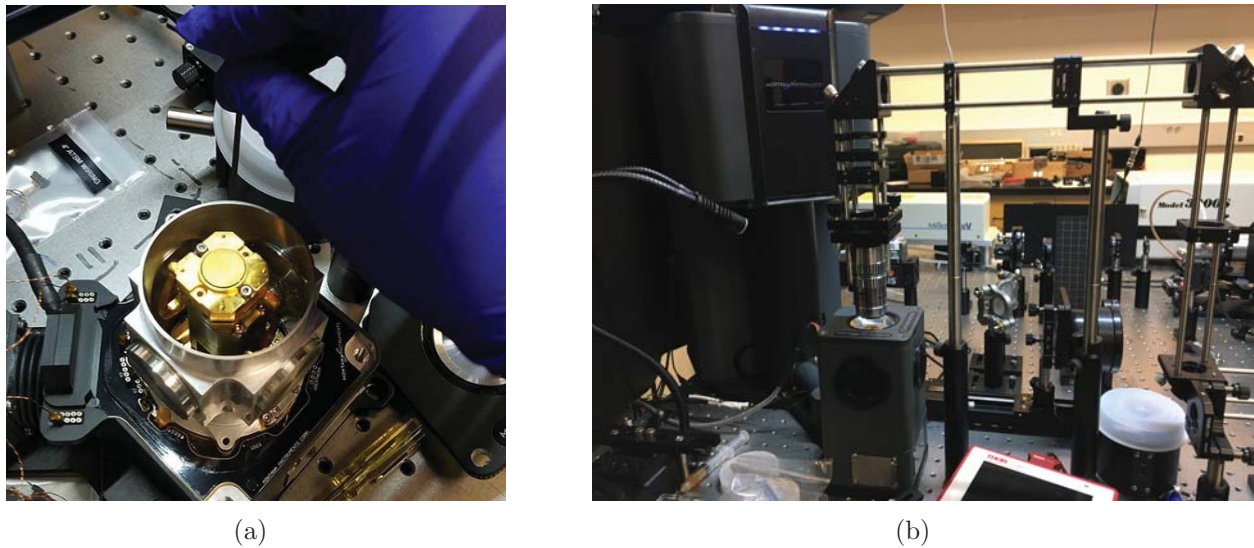


Figure A.8: (a) XYZ stage inside of cryostat. (b) Periscope mount used to probe down into cryostat.

During this time, the blue Obis laser arrived, which we began to incorporate into our system. In order to incorporate the blue laser, we had to change all of the optics in the red path because they were specifically designed for that wavelength. We took this time to completely reorganize the table. The blue pump allowed us to take much better measurements. Later, we purchased a green (532 nm) Obis LX laser to replace the Millenia eV10, which were still using for the probe. The two diode lasers were what allowed us to take really accurate scans for most of the studies because they did not have the noise issues seen with the Millenia eV10. Furthermore, they were also much quieter and smaller. More noise reduction techniques were adopted over time, such as the inclusion of optical isolators and a more efficient polarizer for the EOM. Furthermore, we became more proficient in taking scans in the cryostat, and we learned to be more careful in our beam characterization and scans.

Using the noise reduction techniques and the blue laser, we were able to obtain the reference scans discussed in Chapter 2.3. An FDTR scan of Silicon is shown in Figure A.9.

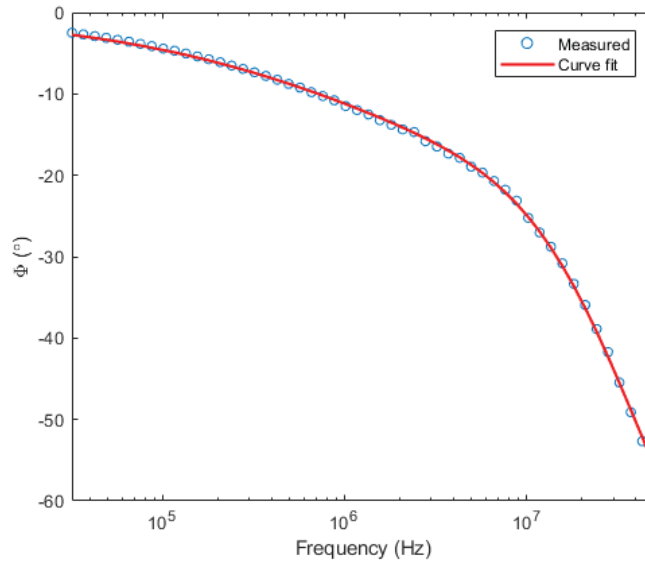


Figure A.9: FDTR scan of Silicon.

At one point, we made a brief decision to change the system back to the red pump, green probe system. This was because we were having trouble taking measurements with the NiTi,

and we believed that it was absorbing too much power from the blue. After spending a couple weeks completely changing all of the optics on the table, we found even more problems than before, including some of the old noise issues. We would ultimately move back to the blue pump, green probe system, again requiring a change in all of the optics.

For the superlattice study, we had to make changes to the optical table again to incorporate the red path, although this time, it was used for the probe. This was done by creating a separate path that only intercepted the old probe path at the dichroic mirror. This allowed us to easily change probe wavelength in less than an hour by changing only a few mirrors. Also, we decided to use a completely new photodetector for this red path, again reducing the number of optics required to change probe color. Figure A.10 is an image of the setup at the time of this report.



Figure A.10: Optical Table at the time of this report.

After the completion of this project, the entire FDTR system will be rebuilt. This will be done to simplify the system for future students to use. Furthermore, we intend to program the XY stage for the purpose of thermal imaging microscopy, which would allow us to probe small features such as individual grains. The intention is for the creation of a simple graphic user interface that would automate scans and analysis.

Appendix B Projected Publications and Presentations

B.1 Projected Publications

1. Warzoha, R.J, Donovan, B.F., **Vu, N.T.**, Champlain, J., Mack, S. and Ruppalt, L., “Nanoscale Thermal Transport in Amorphous and Crystalline GeTe Thin-Films”, Under Review in Applied Physics Letters.
2. Donovan, B.F., Warzoha, R., Venkatesh, R.B., **Vu, N.T.**, Wallen, J. and Lee, D., “Elimination of Extreme Boundary Scattering via Polymer Thermal Bridging in Silica Nanoparticle Thin-Films,” Submitted to Nano Letters.
3. **Vu, N.T.**, Warzoha, R., Donovan, B.F., Sharar, D., Cimpoiasu, E., Leff, A., Wilson, A. and Smith, A.N., “Grain Size-dependent Thermal Transport Properties in NiTi Shape Memory Alloys across the Austenite-Martensite Phase Transition,” To be Submitted to ACS Applied Electronic Materials.
4. Donovan, B.F., Warzoha, R.J., Soule, I., **Vu, N.T.**, Smith, A.N., Koehler, A. and Tajder, M., “Giant Thermal Rectification via Nanocrystalline Diamond Membranes,” To be Submitted to Science.
5. Donovan, B.F., Borgdorff, A., Giri, A., **Vu, N.T.** and Warzoha, R.J., “Thermal Anisotropy in Strained Polymers,” To be Submitted to ACS Applied Materials & Interfaces.
6. **Vu, N.T.**, Wilson, A., Warzoha, R.J., Leff, A. and Taylor, P., “Extreme Thermal Anisotropy in Bi₂Te₃ Nanoscale Thin-Films,” In Preparation.
7. Warzoha, R.J., Donovan, B.F., **Vu, N.T.**, An, L., Clark, A., Cheng, X and Feng, G., “Ultra-high Frequency Domain Thermorefectance for Measurements of Thermal Boundary Conductance at SiO₂-substrate Interfaces,” In Preparation.

B.2 Conference Presentations

1. APS March Meeting 2019, Boston, MA, March 7, “Thermal Characterization of Nickel Titanium Shape Memory Alloys via Frequency Domain Thermorefectance.”
2. DEPS Science and Technology Symposium, Destin, FL, April 11, “Grain Size-dependent Thermal Transport in NiTi Shape Memory Alloys for Thermal Storage in DEW Platforms.”
3. The Intersociety Conference on Thermal and Thermomechanical Phenomena in Electronic Systems (iTherm), Las Vegas, NV, May 28-31, “Effect of Grain Size on the Thermal Properties of Nickel-Titanium Shape Memory Alloys across the Martensite-Austenite Phase Transition.”